Supplement of Atmos. Chem. Phys., 22, 10467–10488, 2022
https://doi.org/10.5194/acp-22-10467-2022-supplement


Atmospheric Chemistry and Physics
Open Access
EGU

*Supplement of*

# Investigating the global OH radical distribution using steady-state approximations and satellite data

**Matilda A. Pimlott et al.**

*Correspondence to:* Matilda A. Pimlott (eemap@leeds.ac.uk)

**Supplemental Information**

**Section S1. Comparison of partially sampled (spatial and temporal) and fully sampled satellite data**

Figures S1 and S2 show the comparison between sub-sampled and fully sampled [OH] data estimated by application of S-SSA to satellite-retrieved $H_2O$, $O_3$, CO and $CH_4$ in the 600-700 hPa layer in 2010 and 2017. The sub-sampled satellite data is sampled every 1 in 10 days and 1 in 4 pixels. Here, we test the comparison in a latitude-averaged zonal mean for each month of 2010 and 2017. The monthly mean correlation coefficient between the sub-sampled and fully sampled data ranges between 0.63–1.00 for 2010 (average of 0.89) and 0.58–0.92 for 2017 (average of 0.85). Despite the lower spatio-temporal resolution of the sub-sampled data, the good agreement in 2010 and 2017 (near the start and end of the timeseries used, 2008–2017) suggests that the sub-sampled data can be used with confidence in zonal mean comparisons for other years.

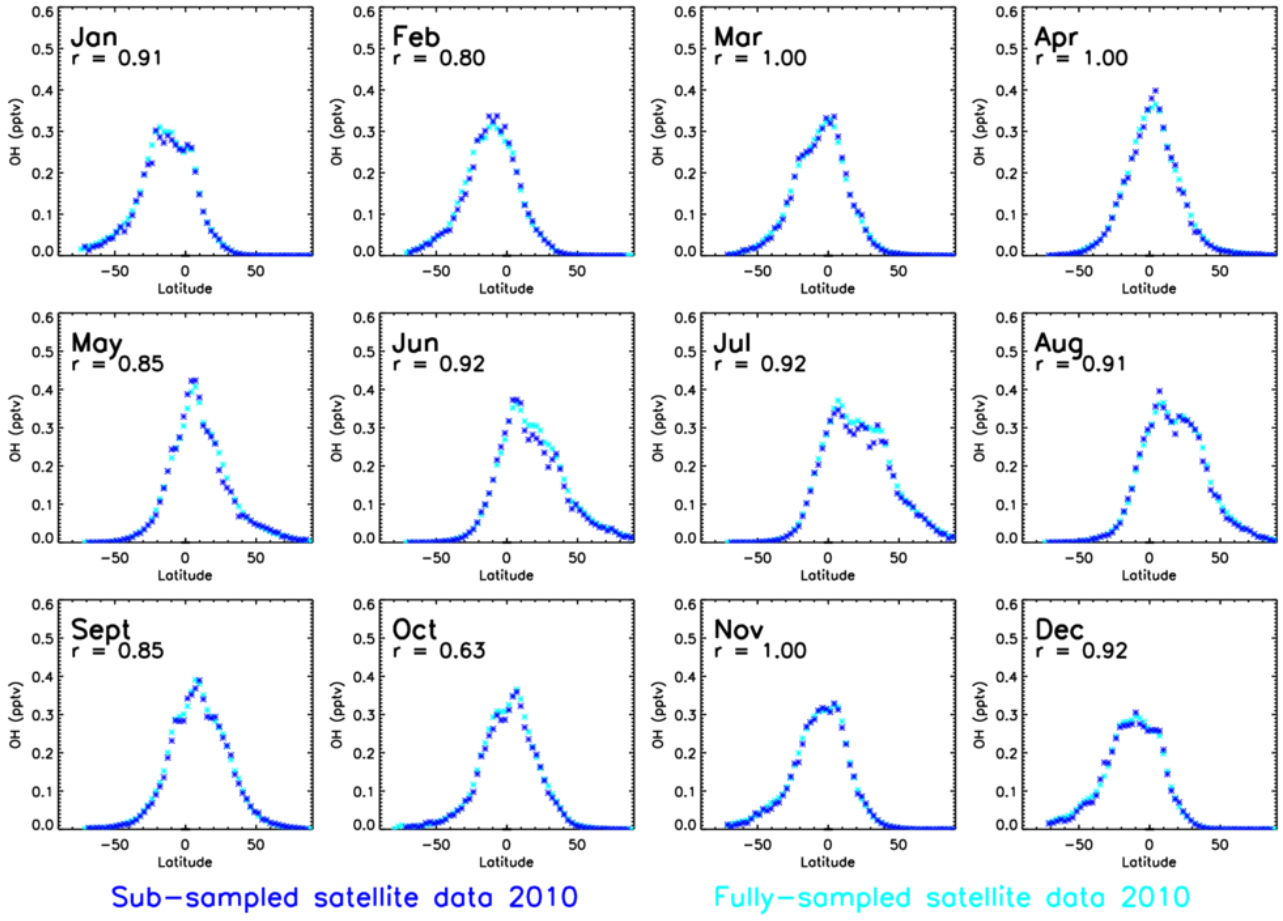

**Figure S1: Zonal mean comparison of S-SSA OH between sub-sampled and fully sampled satellite data in 2010. The dark blue points show latitude-averaged OH for partially sampled data (1 in 10 days and 1 in 4 pixels); the light blue points show the fully sampled data. The Pearson correlation co-efficient (r) is displayed for each month.**

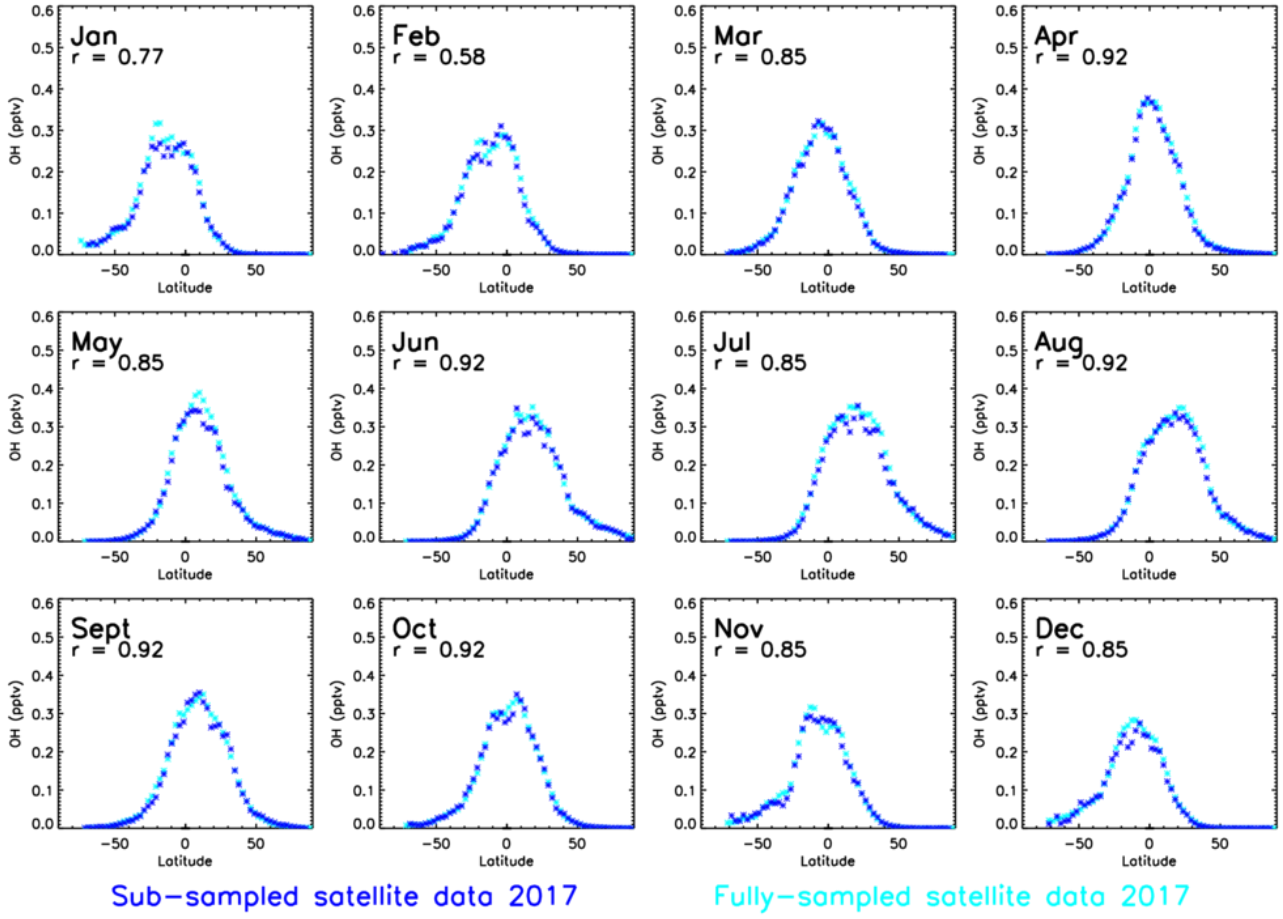


15

**Figure S2: Zonal mean distribution comparison of OH between sub-sampled and fully sampled satellite data in 2017. The dark blue points show latitude-averaged OH for partially sampled data (1 in 10 days and 1 in 4 pixels); the light blue points show the fully sampled data. The Pearson correlation co-efficient (r) is displayed for each month.**

## Section S2. Averaging kernels for $O_3$, CO, $H_2O$ and $CH_4$ data

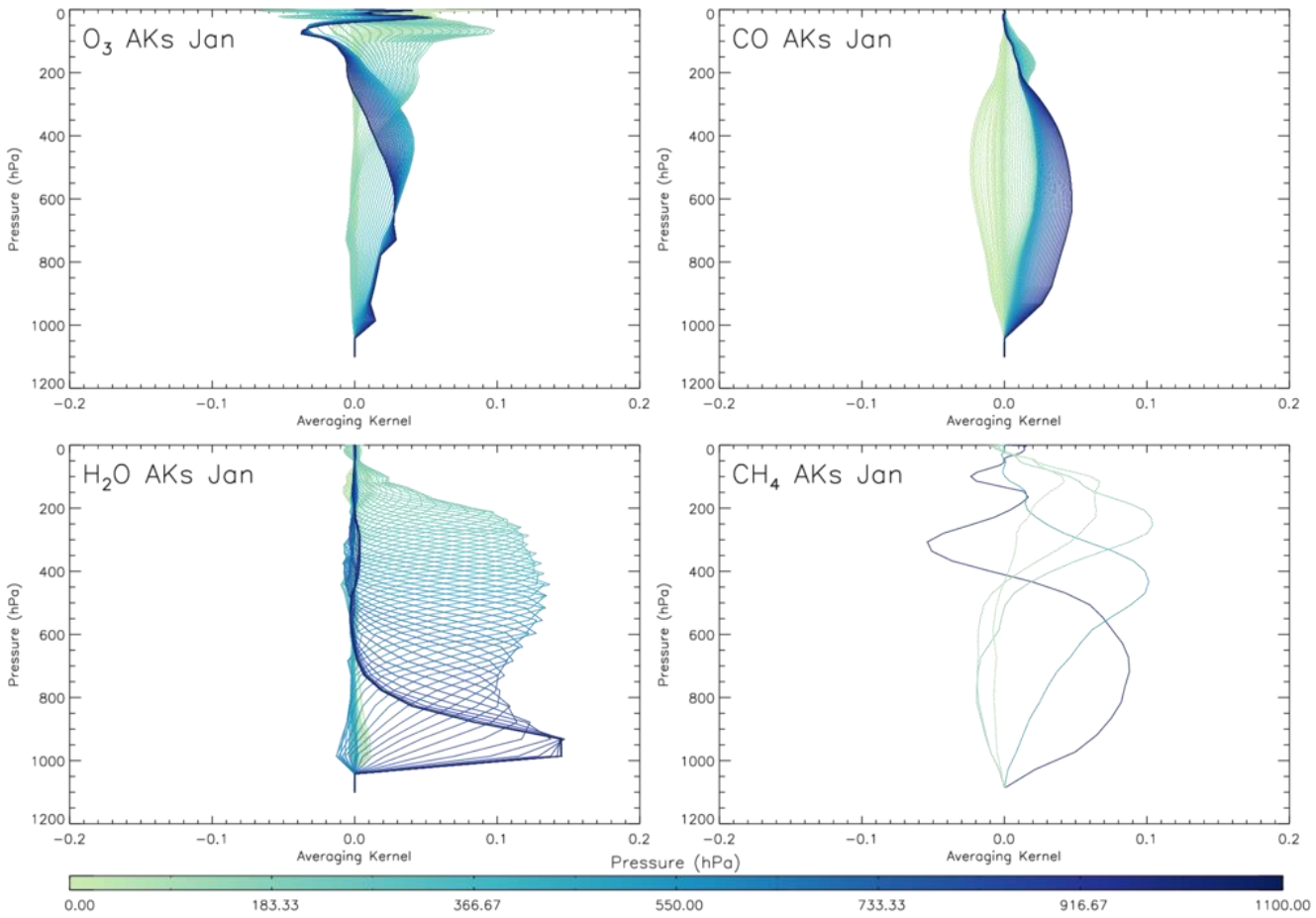


**Figure S3: January 2010 globally averaged vertical averaging kernels (AKs) for retrievals of $O_3$, CO and $H_2O$ from the IMS scheme and $CH_4$ from the IASI scheme.**

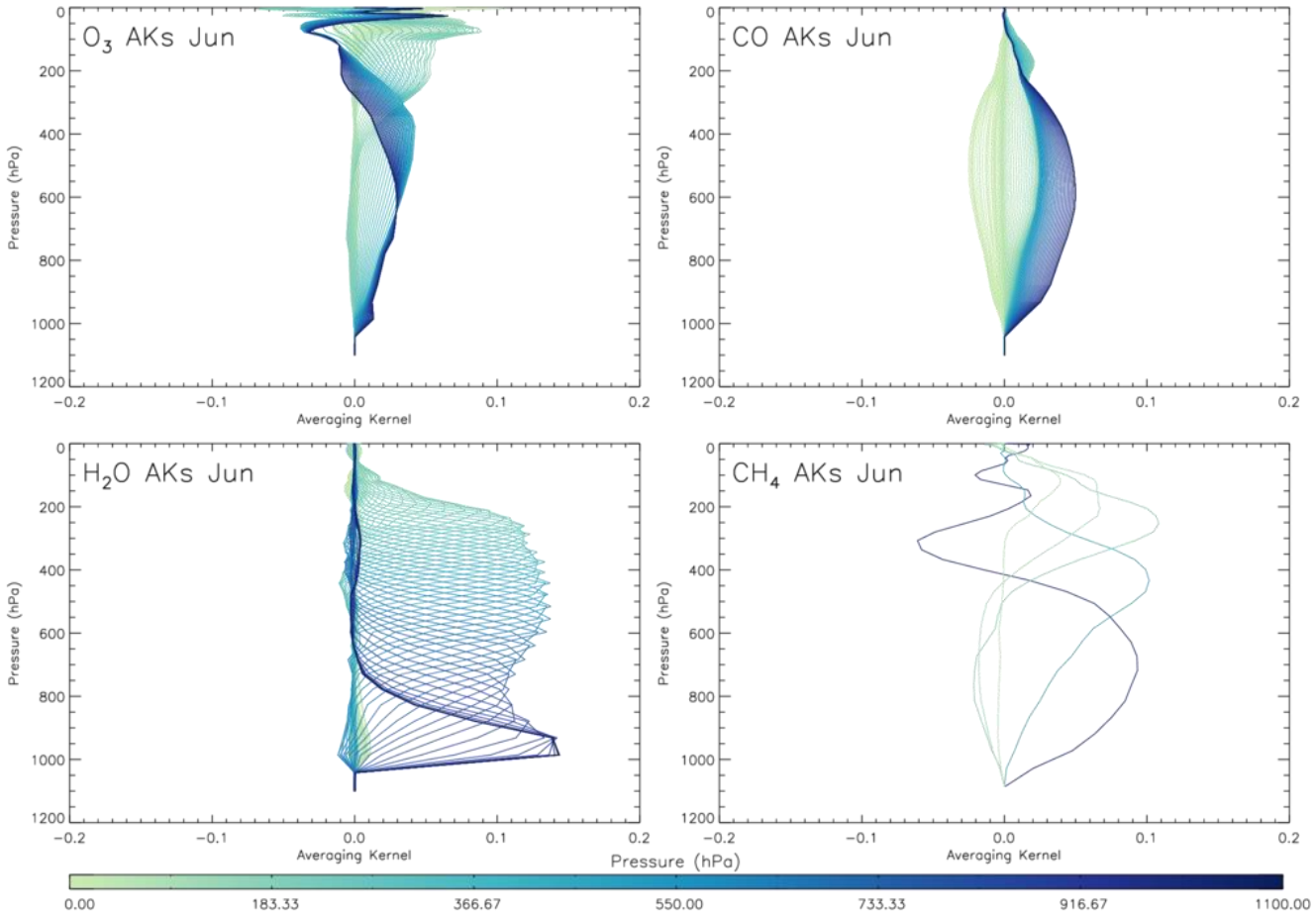


**Figure S4: June 2010 globally averaged vertical averaging kernels (AKs) for retrievals of $O_3$, CO and $H_2O$ from the IMS scheme and $CH_4$ from the IASI scheme.**

**Section S3. Comparison of the IMS retrieved $O_3$ profiles with ozonesondes**

While the $H_2O$, CO and $CH_4$ data used here have been evaluated in previous studies (main manuscript Sect. 2.3.2), $O_3$ data retrieved by the IMS scheme have not. Therefore, we have evaluated IMS $O_3$ data using ozonesondes from the World Ozone and Ultraviolet Radiation Data Centre (WOUDC, https://woudc.org/) and the Southern Hemisphere ADditional OZonesondes (SHADOZ, https://tropo.gsfc.nasa.gov/shadoz) for 2010 and 2017 (i.e. the two fully sampled years of IMS data in the main manuscript). The comparisons are split into three latitude bands (90-30°S, 30°S-30°N and 30-90°N) and four seasons (December-January-February (DJF), March-April-May (MAM), June-July-August (JJA) and September-October-November (SON)). Where suitable ozonesonde profiles exist, they are co-located with the closest $O_3$ retrieval (i.e. within 500 km and 6 hours) and interpolated onto the satellite high-resolution pressure grid. The sonde profiles have an upper limit in the mid-stratosphere so were extended to 0.005 hPa by merging with the retrieval a priori in order to cover the full vertical range spanned by retrieval averaging kernels. A running average was used over several layers in the overlap region to avoid a discontinuity. The following equation (Eq. (S1)) was then applied to the sonde profile to allow a like-for-like comparison between the two quantities by accounting for vertical smearing and the influence of the a priori on the retrieval (Rodgers 2000):

$$\boldsymbol{sonde_{ak} = AK.(sonde_{int} - apr) + apr} \quad \text{(S1)}$$

where $\boldsymbol{AK}$ is the satellite averaging kernel matrix, $\boldsymbol{sonde_{int}}$ is the sonde profile (interpolated onto the satellite pressure grid and extended to 0.005 hPa with the a priori profile), $\boldsymbol{apr}$ is the satellite a priori profile and $\boldsymbol{sonde_{ak}}$ is the sonde profile with the AKs and a priori applied.

Figure S5 shows comparisons between retrieved and sonde profiles averaged in 60° bands for four seasons. We see closest agreement in the Northern Hemisphere (NH) where the sonde sample size largest (>100). Here, the percentage mean bias (MB%) ranges between +4.3 % to +11.0 % in the 600–700 hPa layer. In the tropics, it ranges from +7.4 % to +18.3 % and in the Southern Hemisphere (SH) from +13.1 % to +25.2 %. Overall, the satellite-retrieved profiles have the same vertical structure to that of $sonde_{ak}$, mostly sit within the sonde variability (i.e. 25$^{th}$ to 75$^{th}$ percentile range) and have a reasonably low positive bias of 10 % to 20 %, depending on season and latitude band. For our quantification of errors in the OH budget, we assume a representative relative systematic error of 20 %.

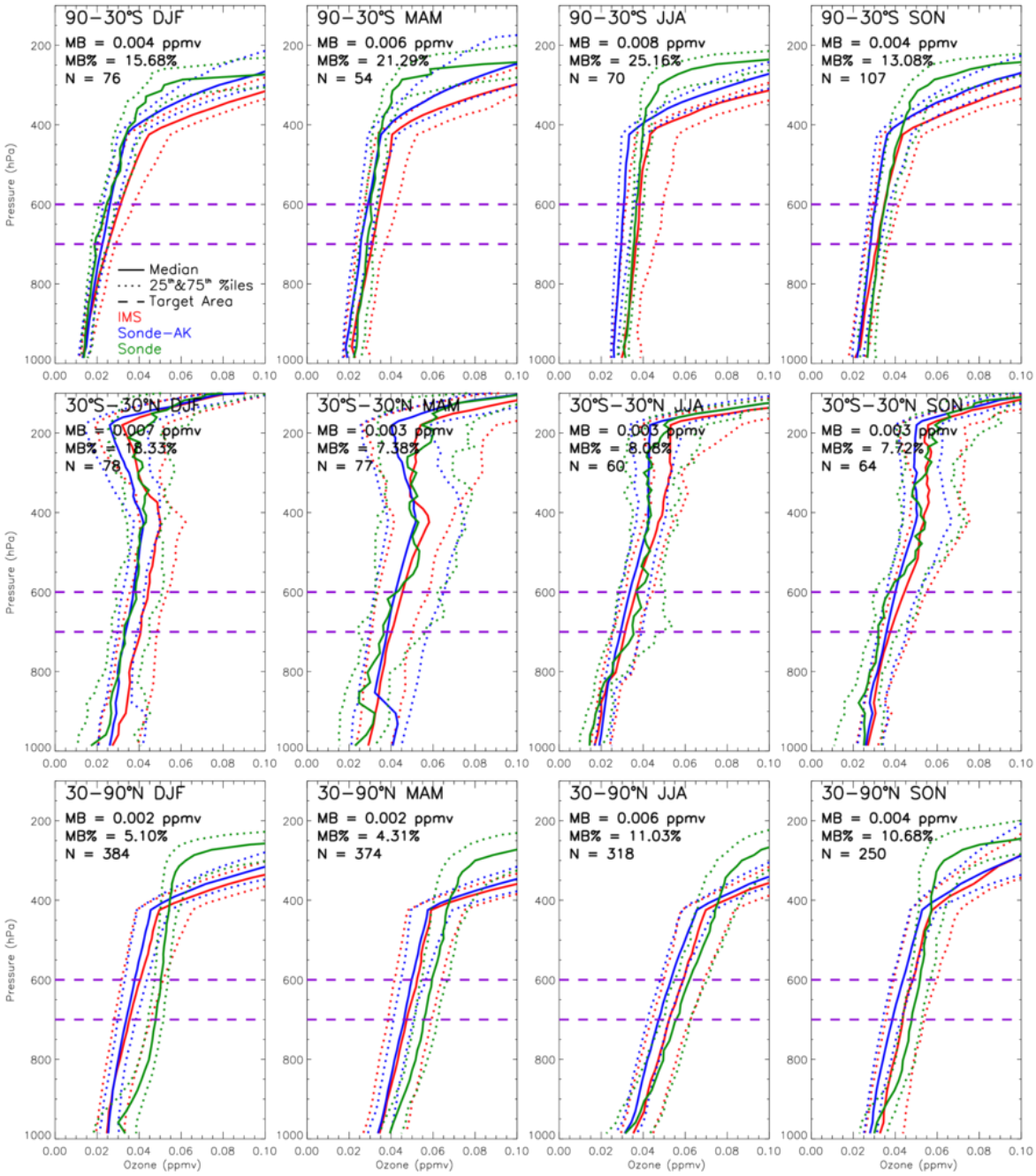


**Figure S5: Comparison of $O_3$ profiles retrieved by the IMS scheme with ozonesonde (WOUDC and SHADOZ) profiles (ppmv) for 2010 and 2017 merged. The regions are split into three latitude bands (90-30°S, 30°S-30°N & 30-90°N) and four seasons (December-January-February (DJF), March-April-May (MAM), June-July-August (JJA) & September-October-November (SON)). Red, blue and green solid (dotted) profiles show the median (25th and 75th percentile) IMS, ozonesonde with IMS averaging kernels applied and ozonesonde profiles. Here, the closest satellite retrieval within 500 km and 6 hours of each ozonesonde profile has been used. The purple dashed lines represent the pressure region of interest (600–700 hPa). The mean bias (MB), percentage bias (MB%), and number of sonde profiles (N) are shown based on the 600–700 hPa segments of the profiles.**

## Section S4. Description of OH source and sink equations used in simplified and complex steady-state approximations

Table S1 lists the source and sink reactions in each approximation used (Savage et al., 2001; Monks et al., 2017).

| Approximation | Source Reactions | Sink Reactions |
|---|---|---|
| Simplified | 1. $O_3 + h\nu$ ($\lambda < 330$ nm) → $O(^1D) + O_2$<br>2. $O(^1D) + H_2O \rightarrow 2OH$ | 1. $CO + OH (+ O_2) \rightarrow CO_2 + HO_2$<br>2. $CH_4 + OH (+ O_2) \rightarrow H_2O + CH_3OO$<br>3. $O_3 + OH \rightarrow HO_2 + O_2$ |
| Savage et al. (2001) | 1. $O_3 + h\nu$ ($\lambda < 330$ nm) → $O(^1D) + O_2$<br>2. $O(^1D) + H_2O \rightarrow 2OH$<br>3. $H_2O_2 + \underline{h\nu} \rightarrow 2OH$<br>4. $CH_3OOH + \underline{h\nu} \rightarrow HO_2 + HCHO + OH$<br>5. $HO_2 + NO \rightarrow OH + NO_2$<br>6. $HO_2 + O_3 \rightarrow OH + 2O_2$ | 1. $CO + OH (+ O_2) \rightarrow CO_2 + HO_2$<br>2. $CH_4 + OH (+ O_2) \rightarrow H_2O + CH_3OO$<br>3. $O_3 + OH \rightarrow HO_2 + O_2$<br>4. $HCHO + OH (+ O_2) \rightarrow H_2O + HO_2 + CO$<br>5. $SO_2 + OH (+ O_2) \rightarrow SO_3 + HO_2$<br>6. $NO_2 + OH + M \rightarrow HONO_2 + M$<br>7. $NO + OH + M \rightarrow HONO + M$<br>8. $DMS + OH \rightarrow$ products<br>9. $H_2O_2 + OH \rightarrow H_2O + HO_2$<br>10. $CH_3OOH + OH \rightarrow H_2O + CH_3OO$<br>11. $H_2 + OH (+ O_2) \rightarrow H_2O + HO_2$<br>12. $C_2H_4 + OH + M \rightarrow C_3H_7OOO + M$<br>13. $C_2H_6 + OH \rightarrow H_2O + EtOO$<br>14. $C_3H_6 + OH + M \rightarrow C_3H_7OOO + M$<br>15. $C_3H_8 + OH \rightarrow$ n-$PrOO + H_2O$<br>16. $C_3H_8 + OH \rightarrow$ i-$PrOO + H_2O$<br>17. $C_4H_{10} + OH \rightarrow C_4H_{10}OO + H_2O$<br>18. $C_5H_8 + OH \rightarrow ISO_2$<br>19. $C_{10}H_{16} + OH \rightarrow TERPO_2$ |

| | | |
|---|---|---|
| Complex | 1. $O_3 + h\nu$ ($\lambda < 330$ nm) → $O(^1D) + O_2$<br>2. $O(^1D) + H_2O \rightarrow 2OH$<br>3. $HO_2 + NO \rightarrow OH + NO_2$<br>4. $HO_2 + NO_3 \rightarrow OH + NO_2$<br>5. $HO_2 + O_3 \rightarrow OH + O_2$<br>6. $HO_2 + CH_3CO_3 \rightarrow OH + CH_3OO$<br>7. $O(^1D) + CH_4 \rightarrow OH + CH_3OO$<br>8. $O_3$ + MACR → $CH_3C(O)CHO + HCOOH + HO_2 + CO + OH + CH_3CO_3$<br>9. $O_3 + C_{10}H_{16} \rightarrow OH + CH_3COCH_2CH_3 + HO_2$<br>10. $C_2H_4 + O_3 \rightarrow HCHO + HO_2 + OH + CO + H_2 + CO_2 + HCOOH$<br>11. $C_3H_6 + O_3 \rightarrow HCHO + CH_3CHO + OH + HO_2 + C_2H_5OO + CH_3C(O)CHO + CH4 + CO + CH_3OH + CH_3OO + HCOOH$<br><br>Photolysis reactions:<br>12. $C_2H_5OOH + h\nu \rightarrow CH_3CHO + HO_2 + OH$<br>13. $H_2O_2 + h\nu \rightarrow OH + OH$<br>14. $HONO_2 + h\nu \rightarrow OH + NO_2$<br>15. $CH_3OOH + h\nu \rightarrow HO_2 + HCHO + OH$<br>16. $HONO + h\nu \rightarrow OH + NO$<br>17. $C_3H_7OOH + h\nu \rightarrow C_2H_5CHO + HO_2 + OH$<br>18. $C_3H_7OOH + h\nu \rightarrow (CH_3)_2CO + HO_2 + OH$<br>19. $CH_3COCH_2OOH + h\nu \rightarrow CH_3CO_3 + HCHO + OH$<br>20. TERPOOH + $h\nu$ → $OH + HO_2$ + MACR + MACR + TERPOOH + $(CH_3)_2CO$<br>21. ISOOH + $h\nu$ → OH + MACR + HCHO + $HO_2$<br>22. MACROOH + $h\nu \rightarrow OH + HO_2 + OH + HO_2$ + HAC + CO + $CH_3C(O)CHO$ + HCHO<br>23. $CH_3CO_3H + h\nu \rightarrow CH_3OO + OH$<br>24. $C_4H_{10}OOH + h\nu \rightarrow CH_3COCH_2CH_3$ + | 1. $CH_4 + OH (+ O_2) \rightarrow H_2O + CH_3OO$<br>2. $C_2H_6 + OH (+ O_2) \rightarrow H_2O + C2H_5OO$<br>3. $C_3H_8 + OH (+ O_2) \rightarrow$ n-PrOO + $H_2O$<br>4. $C_3H_8 + OH (+ O_2) \rightarrow$ i-PrOO + $H_2O$<br>5. $CO + OH (+ O_2) \rightarrow CO_2 + HO_2$<br>6. $C_2H_5CHO + OH \rightarrow H_2O + C_2H_5CO_3$<br>7. $C_2H_5OOH + OH \rightarrow H_2O + C_2H_5OO$<br>8. $H_2 + OH (+ O_2) \rightarrow H_2O + HO_2$<br>9. $H_2O_2 + OH \rightarrow H_2O + HO_2$<br>10. $HCHO + OH (+ O_2) \rightarrow H_2O + HO_2 + CO$<br>11. $HO_2 + OH \rightarrow H_2O (+ O_2)$<br>12. $HO_2NO_2 + OH \rightarrow H_2O + NO_2$<br>13. $HO_2NO_2 + OH \rightarrow H_2O + NO_3$<br>14. $HONO + OH \rightarrow H_2O + NO_2$<br>15. $CH_3OOH + OH \rightarrow H_2O + CH_3OO$<br>16. $CH_3ONO_2 + OH \rightarrow HCHO + NO_2 + H_2O$<br>17. $(CH_3)_2CO + OH \rightarrow H_2O + CH_3COCH_2OO$<br>18. $CH_3COCH_2OOH + OH \rightarrow H_2O + CH_3COCH_2OO$<br>19. $CH_3CHO + OH \rightarrow H_2O + CH_3CO_3$<br>20. $NO_3 + OH \rightarrow HO_2 + NO_2$<br>21. $O_3 + OH \rightarrow HO_2 + O_2$<br>22. PAN + OH → HCHO + $NO_2$ + $H_2O$<br>23. PPAN + OH → $CH_3CHO + NO_2 + H_2O$<br>24. n-$C_3H_7OOH$ + OH → n-$C_3H_7OO$ + $H_2O$<br>25. i-$C_3H_7OOH$ + OH → i-$C_3H_7OO$ + $H_2O$<br>26. $C_5H_8 + OH \rightarrow ISO_2$<br>27. ISON + OH → $CH_3C(O)CH_2OH$ + NALD<br>28. MACR + OH → $MACRO_2$<br>29. MPAN + OH → $CH_3C(O)CH_2OH + NO_2$<br>30. MACROOH + OH → $MACRO_2$<br>31. $CH_3C(O)CH_2OH + OH \rightarrow CH_3C(O)CHO + HO_2$<br>32. $CH_3C(O)CHO + OH \rightarrow CH_3CO_3 + CO$ |

| | | |
|---|---|---|
| | $CH_3COCH_2CH_3 + C_2H_5OO + CH_3CHO + HO_2 + HO_2 + OH + OH + OH$<br>25. $CH_3COCH_2CH_3OOH + h\nu \rightarrow CH_3CO_3 + CH_3CHO + OH$<br>26. $AROMOOH + h\nu \rightarrow OH + (CH_3)_2CO + HO_2 + CO + CH_3CO_3 + AROMOOH$ | 33. $NALD + OH \rightarrow HCHO + CO + NO_2$<br>34. $CH_3CO_3H + OH \rightarrow CH_3CO_3$<br>35. $CH_3CO_2H + OH \rightarrow CH_3OO$<br>36. $HCOOH + OH \rightarrow HO_2$<br>37. $CH_3OH + OH \rightarrow HCHO + HO_2$<br>38. $C_{10}H_{16} + OH \rightarrow TERPO_2$<br>39. $TERPOOH + OH \rightarrow TERPO_2$<br>40. $C_4H_{10} + OH \rightarrow C_4H_{10}OO + H_2O$<br>41. $CH_3C(O)CH_2CH_3 + OH \rightarrow CH_3C(O)CH_2CH_3OO$<br>42. $ONIT + OH \rightarrow CH_3C(O)CH_2CH_3 + NO_2 + H_2O$<br>43. $C_3H_7OOOH + OH \rightarrow C_3H_7OOO + H_2O$<br>44. $AROM + OH \rightarrow AROMO_2 + HO_2$<br>45. $AROMOOH + OH \rightarrow AROMO_2$<br>46. $NO + OH + M \rightarrow HONO + M$<br>47. $NO_2 + OH \rightarrow HONO_2 + M$<br>48. $C_2H_4 + OH + M \rightarrow C_3H_7OOO + M$<br>49. $C_3H_6 + OH + M \rightarrow C_3H_7OOO + M$ |

**Table S1: List of source and sink reactions of OH for each steady-state approximation. MACR represents a lumped species (methacrolein, methyl vinyl ketone and other C4 carbonyls), $ISO_2$ represents peroxy radicals from the reaction of isoprene and OH (Pöschl et al., 2000), TERP represents generic terpene compound, NALD represents nitroxy acetaldehyde, ONIT represents organic nitrate and AROM represents a generic aromatic compound (Monks et al., 2017).**

**Section S5. Number of satellite retrievals**

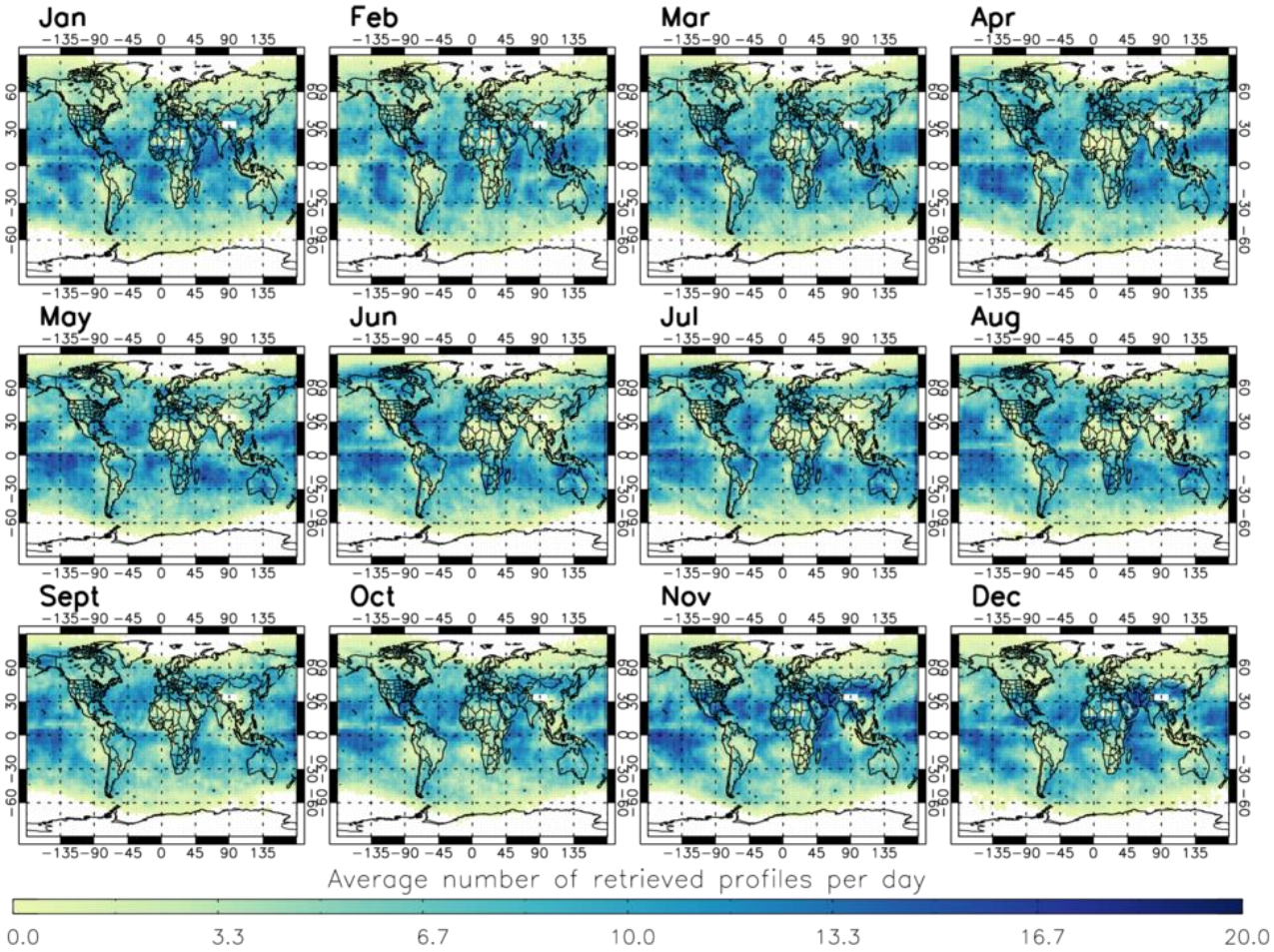


**Figure S6: Average daily number of retrieved profiles of the input species ($O_3$, CO, $CH_4$ & $H_2O$) used the in OH calculation for each grid box for each month in 2010.**

**Section S6. Satellite OH uncertainty calculation**

An uncertainty estimate for the satellite S-SSA OH is derived using relative systematic errors for each of the four retrieved quantities: ~10 % for CO (Pope et al., 2021), ~10 % for $H_2O$ (available soon at: https://climate.esa.int/en/projects/water-vapour/key-documents/), ~20 % for $O_3$ (see Supplementary Sect. S3) and an average of 0.55 % for $CH_4$ (Siddans et al., 2017). Large-scale averaging in the analysis reported here reduces random errors to values which are very small by comparison. The error on OH calculated according to the S-SSA combines the systematic components based on the following equations:

$$For\ a = b + c\ \ then\ (\Delta a)^2 = (\Delta b)^2 + (\Delta c)^2 \quad \text{(S2)}$$

$$For\ a = bc\ or\ a = b/c\ \ then\ \left(\frac{\Delta a}{a}\right)^2 = \left(\frac{\Delta b}{b}\right)^2 + \left(\frac{\Delta c}{c}\right)^2 \quad \text{(S3)}$$

where $b$ and $c$ are variables and $\Delta a$ indicates the uncertainty of $a$ etc. (Hogan, 2006). To calculate the uncertainty on OH, the uncertainties on the numerator and denominator of Eq. (4) in the main manuscript, are calculated and then combined using Eq. (S3). Here, we assume there is no uncertainty in the rate constants ($j_1$, $k_{1\text{-}6}$) (see below) and errors on the retrieved species are assumed to be uncorrelated.

The numerator is defined as follows:

$$\alpha = 2\, j_1\, k_1\, [H_2O]\, [O_3], \quad \text{(S4)}$$

$$\beta = k_2\, [N_2] + k_3\, [O_2] + k_1\, [H_2O], \quad \text{(S5)}$$

$$\gamma = \frac{\alpha}{\beta}. \quad \text{(S6)}$$

Uncertainty in the numerator (γ) is calculated as follows, using Eqs. (S2 and S3):

$$\left(\frac{\Delta\gamma}{\gamma}\right)^2 = \left(\frac{\Delta\alpha}{\alpha}\right)^2 + \left(\frac{\Delta\beta}{\beta}\right)^2, \quad \text{(S7)}$$

$$\left(\frac{\Delta\alpha}{\alpha}\right)^2 = \left(\frac{\Delta[H_2O]}{[H_2O]}\right)^2 + \left(\frac{\Delta[O_3]}{[O_3]}\right)^2, \quad \text{(S8)}$$

$$(\Delta\beta)^2 = (\Delta k_1[H_2O])^2, \quad \text{(S9)}$$

$$\left(\frac{\Delta\beta}{\beta}\right)^2 = \frac{(\Delta k_1[H_2O])^2}{(k_2\,[N_2]+k_3\,[O_2]+k_1\,[H_2O])^2}. \quad \text{(S10)}$$

Uncertainty in the denominator (δ) is calculated as follows using Eq. (S2):

$$\delta = k_4\,[CH_4] + k_5\,[CO] + k_6\,[O_3], \quad \text{(S11)}$$

$$(\Delta\delta)^2 = (\Delta k_4[CH_4])^2 + (\Delta k_5[CO])^2 + (\Delta k_6[O_3])^2, \quad \text{(S12)}$$

$$\left(\frac{\Delta\delta}{\delta}\right)^2 = \frac{(\Delta k_4[CH_4])^2 + (\Delta k_5[CO])^2 + (\Delta k_6[O_3])^2}{(k_4\,[CH_4] + k_5\,[CO] + k_6\,[O_3])^2}. \quad \text{(S13)}$$

Uncertainty in [OH] is then calculated as follows using Eq. (S3):

$$\Delta[OH] = \sqrt{\left(\frac{\Delta\alpha}{\alpha}\right)^2 + \left(\frac{\Delta\beta}{\beta}\right)^2 + \left(\frac{\Delta\delta}{\delta}\right)^2} \times [OH]. \quad \text{(S14)}$$

Figure S7 shows the estimated uncertainty of OH for each month of 2010. This corresponds to a typical relative uncertainty of ~23 %.

This method assumes there is no uncertainty in the rate constants. We have compared TOMCAT and ATom observed $j_1$ in Fig. S8, to see if this assumption is reasonable. $j_1$ is low compared to the ATom observations, with a mean bias ranging between -0.09 and -1.29 $\times 10^{-5}$ $s^{-1}$ across the 4 campaigns. There are a few notable areas of disagreement, such as near the equator in ATom-2, between 60°S and 20°S in ATom-3, between the equator to 20°N in ATom-4 and between 40°N to 60°N in ATom-4. However, due to the difficulties in the comparison of the two datasets, the agreement can be considered as reasonable.

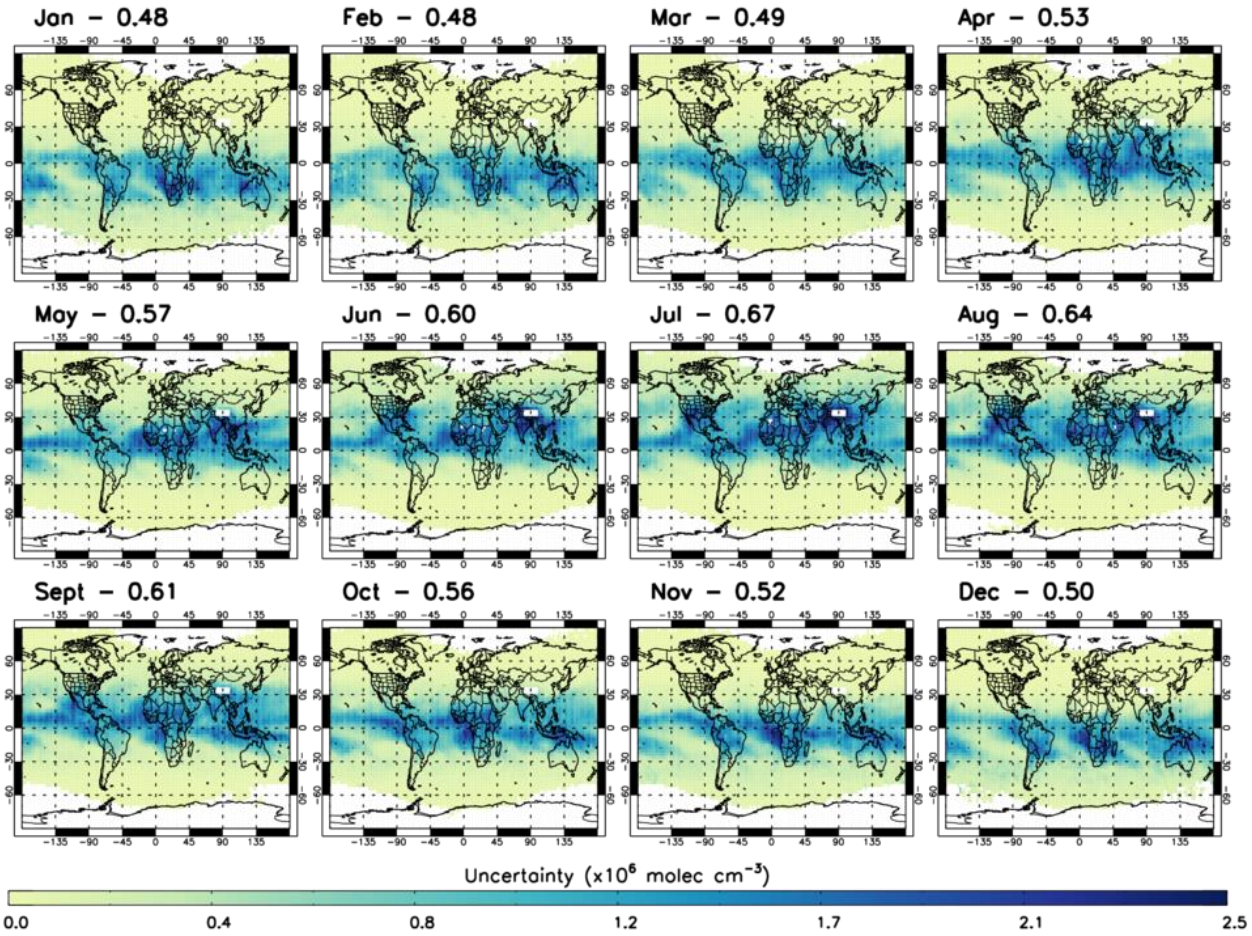


**Figure S7: Estimated uncertainty for satellite S-SSA OH for all months of 2010 in units of ×10$^6$ molecule cm$^{-3}$. Global mass-weighted mean estimated uncertainty in OH (×10$^6$ molecule cm$^{-3}$) are labelled for each month**

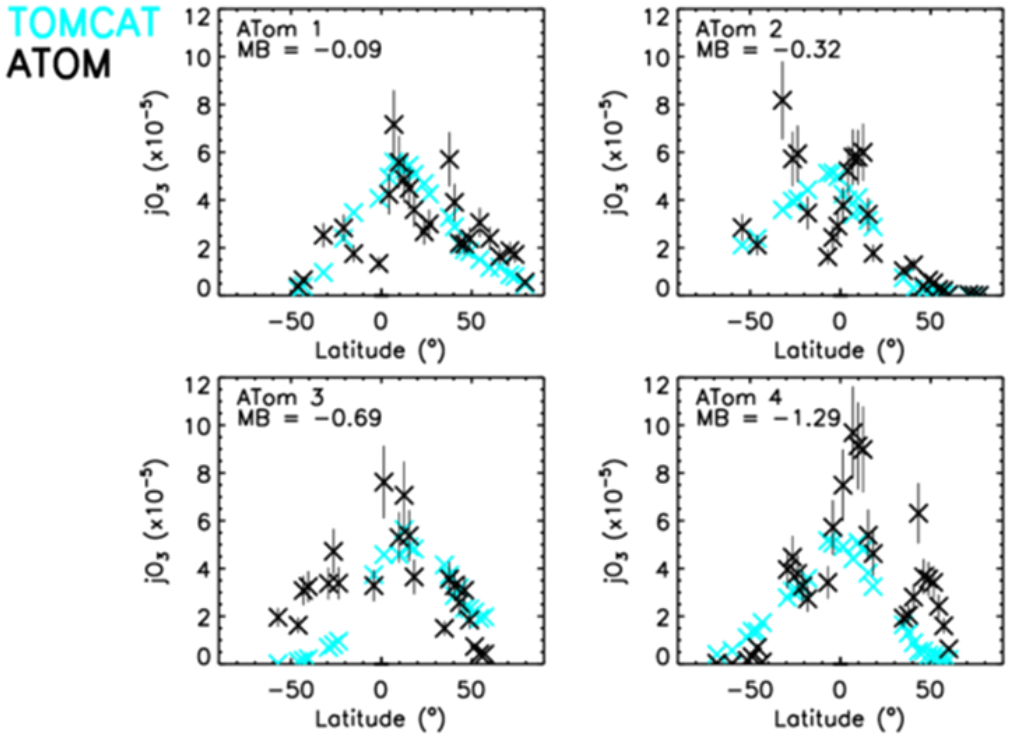


**Figure S8: Comparison between TOMCAT $j_{O_3}$ values and ATom $j_{O_3}$ observations, averaged for each model latitude bin. The four panels show the data split into the individual campaigns. ATom observations are filtered for 600–700 hPa and 08:00–11:00 LT. All data is in units of $\times 10^{-5}$ $s^{-1}$. The mean bias (calculated from TOMCAT - ATom) are displayed in the top left corner of each panel. Error bars of ± 20 % (representing the instrument uncertainty (Shetter and Müller, 1999)) are displayed for each ATom observation.**

**Section S7. Application of TOMCAT and satellite data from 2017 to the S-SSA**

Figure S9 shows a latitude-averaged plot of TOMCAT OH and TOMCAT S-SSA OH in 2017 (similar to Fig. 1 for 2010 in the main manuscript). Table S2 shows that the largest differences between mean TOMCAT OH and TOMCAT S-SSA OH occur at pressures less than 400 hPa (upper troposphere and above). Nearer the surface (> 800 hPa) there is a good zonal mean agreement (< 6%), however large differences are present in a 2D spatial plot and the complex OH chemistry here is unlikely to be captured by the simplified approximation. The mid tropospheric region, between 400–800 hPa shows a good agreement, an underestimate here of 31-34 %, with the better agreement between 600–700 hPa of ~ 27%.

Figure S10 shows a comparison of OH global monthly mean maps in January and June 2017 for the 600–700 hPa layer as calculated by TOMCAT, TOMCAT FC-SSA, TOMCAT S-SSA and satellite S-SSA. TOMCAT and TOMCAT FC-SSA show very similar spatial patterns and global weighted averages (~ 6 % difference) in both January and June. The satellite S-SSA distributions agree best with TOMCAT S-SSA, as might be expected. Agreement between the satellite S-SSA distribution and the three TOMCAT distributions is somewhat better in January than June. In January, the satellite S-SSA and three TOMCAT distributions have similar peaks over NW Australia and S Africa e.g. TOMCAT OH 16.5 $\times 10^6$ molecule $cm^{-3}$ and satellite OH 14.0 $\times 10^6$ molecule $cm^{-3}$. The global weighted average OH values compare well in January, with TOMCAT OH at 2.88 $\times 10^6$ molecule $cm^{-3}$ and satellite OH ~21 % less at 2.27 $\times 10^6$ molecule $cm^{-3}$. In June, the satellite S-SSA OH again shows a similar spatial distribution to the other three TOMCAT datasets with peaks over S Asia, N Africa and N America. The global mean satellite S-SSA value for June is 2.70 $\times 10^6$ molecule $cm^{-3}$, which is 28 % lower than the TOMCAT OH value of 3.76 $\times 10^6$ molecule $cm^{-3}$.

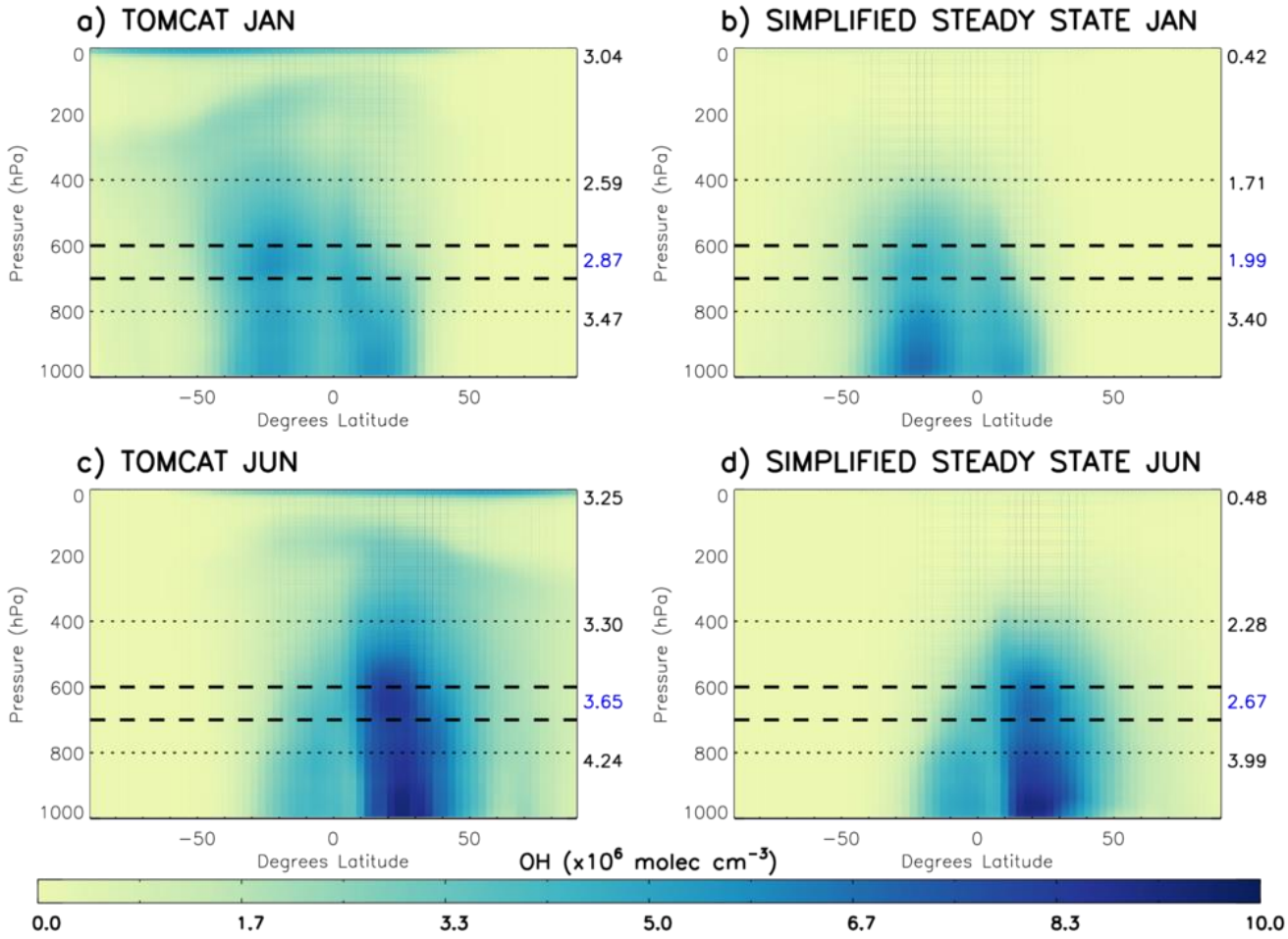


155 **Figure S9: Comparison of TOMCAT OH and S-SSA OH: (a) TOMCAT OH January 2017, (b) TOMCAT S-SSA OH January 2017, (c) TOMCAT OH June 2017, (d) TOMCAT S-SSA OH June 2017. The dashed lines represent the selected pressure range of best agreement, 600–700 hPa. The numbers of the right of each panel represent the mean OH of the region in $\times 10^6$ molecule $cm^{-3}$ (from top to bottom): pressures less than 400 hPa, between 400–800 hPa and greater than 800 hPa.**

| | **S-SSA OH average - TOMCAT OH average ($\times 10^6$ molecule $cm^{-3}$)** | |
|---|---|---|
| **Pressure range** | January | June |
| < 400 hPa | -2.62 (-86 %) | -2.77 (-85 %) |
| 400–800 hPa | -0.88 (-34 %) | -1.02 (-31 %) |
| > 800 hPa | -0.07 (-2 %) | -0.25 (-6 %) |
| 600–700 hPa | -0.88 (-31 %) | -0.98 (-27 %) |

**Table S2: Comparison of global mean TOMCAT OH and S-SSA OH for different pressure ranges. Percentage difference relative to the TOMCAT OH mean given in brackets.**

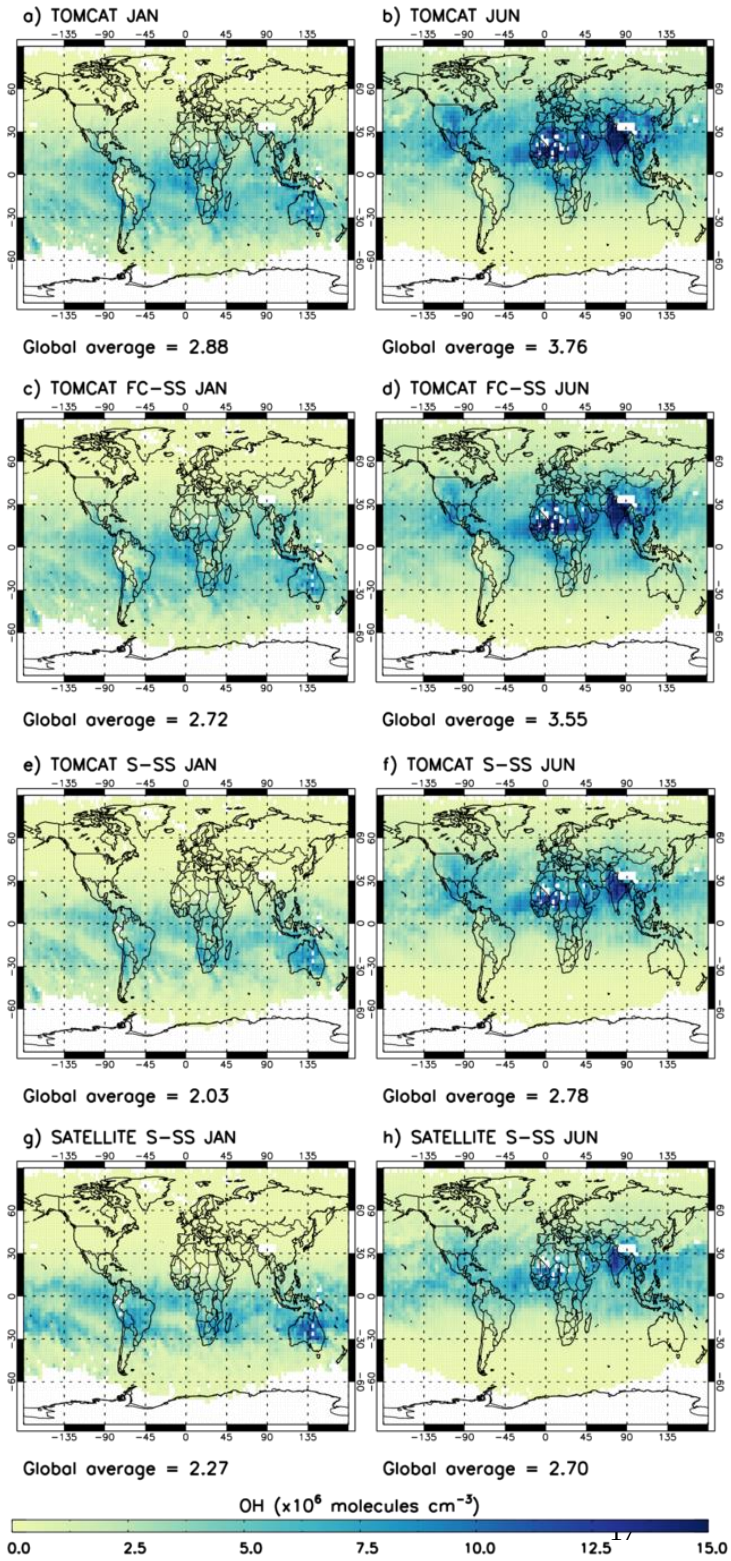


**Figure S10: 2017 OH comparison for the 600–700 hPa layer. (a) TOMCAT January, (b) TOMCAT June, (c) TOMCAT FC-SSA January, (d) TOMCAT FC-SSA June, (e) TOMCAT S-SSA January, (f) TOMCAT S-SSA June, (g) Satellite S-SSA January and (h) Satellite S-SSA June. Global mean OH values ($\times 10^6$ molecule $cm^{-3}$) for this pressure range are given below each panel.**

**Section S8. Contribution of source and sink terms to the OH steady-state approximation from Savage et al. (2001)**

We apply TOMCAT model data to two more complex steady-state approximations, FC-SSA and Sav-SSA. The application of these expressions can indicate which atmospheric species are key to OH production and removal in different regions of the atmosphere. For the underestimate of the S-SSA at pressures less than 400 hPa, Fig. S11 and Fig. S12, using the Sav-SSA show that an important source in this region is the reaction of nitric oxide (NO) and the hydroperoxyl radical ($HO_2$). The OH and $HO_2$ radicals are closely linked in chemical cycles which are not, however, represented in the S-SSA. There are no NO or $HO_2$ satellite observations available in the relevant altitude range, so we cannot include this term in the S-SSA. The current source term, photolysis of ozone and subsequent reaction of the photo-generated $O(^1D)$ atoms with $H_2O$, is controlled above the tropopause by the amount of $H_2O$, which is much lower than in the troposphere. The lack of other sources included in the S-SSA, at lower pressures above the tropopause, where these other sources would dominate the production of OH, yields an underestimation in OH.

For the overestimate by the S-SSA between 800 hPa and the surface, Fig. S15 and Fig. S16 show that there are a number of important sink reactions for OH which are not included in the S-SSA, but are included in the Sav-SSA. These sink species include nitrogen dioxide ($NO_2$), dimethyl sulphide (DMS), hydrogen ($H_2$), hydrogen peroxide ($H_2O_2$), NO, sulphur dioxide ($SO_2$), formaldehyde (HCHO) and a combination of hydrocarbons (e.g. alkanes and alkenes). These additional sink terms could potentially help reduce the overestimate of the S-SSA in this region, however satellite data for some of these species is not available in the relevant pressure region, and for others e.g. HCHO, $NO_2$ and $SO_2$ it is not available from a similar instrument to the species in the S-SSA.

Figures S11–16 show the contribution of different source and sink terms in the Savage et al. (2001) approximation (Sav-SSA) to the overall source and sink term.

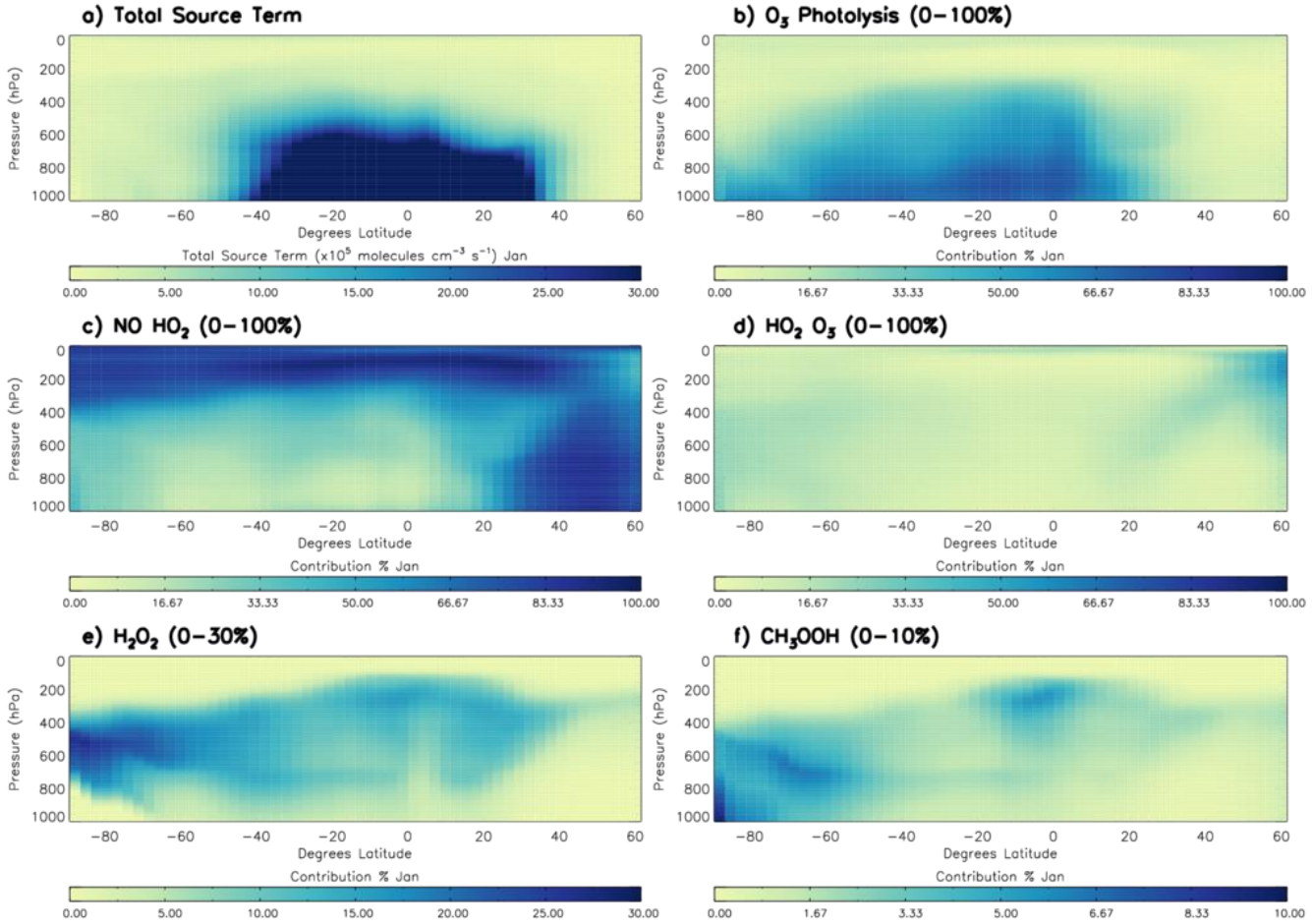


205

**Figure S11: January 2010 zonal mean global plots showing the total source term from the Sav-SSA and the different components as a % of total. The terms are: (a) total source, (b) photolysis of $O_3$ to form $O(^1D)$ which reacts with $H_2O$ for form OH, (c) reaction of NO and $HO_2$, (d) reaction of $HO_2$ and $O_3$, (e) photolysis of $H_2O_2$ and (f) photolysis of $CH_3OOH$. The data is presented from 90° S–60° N due to several species being zero above 60° N because of polar night at these latitudes during January.**

210

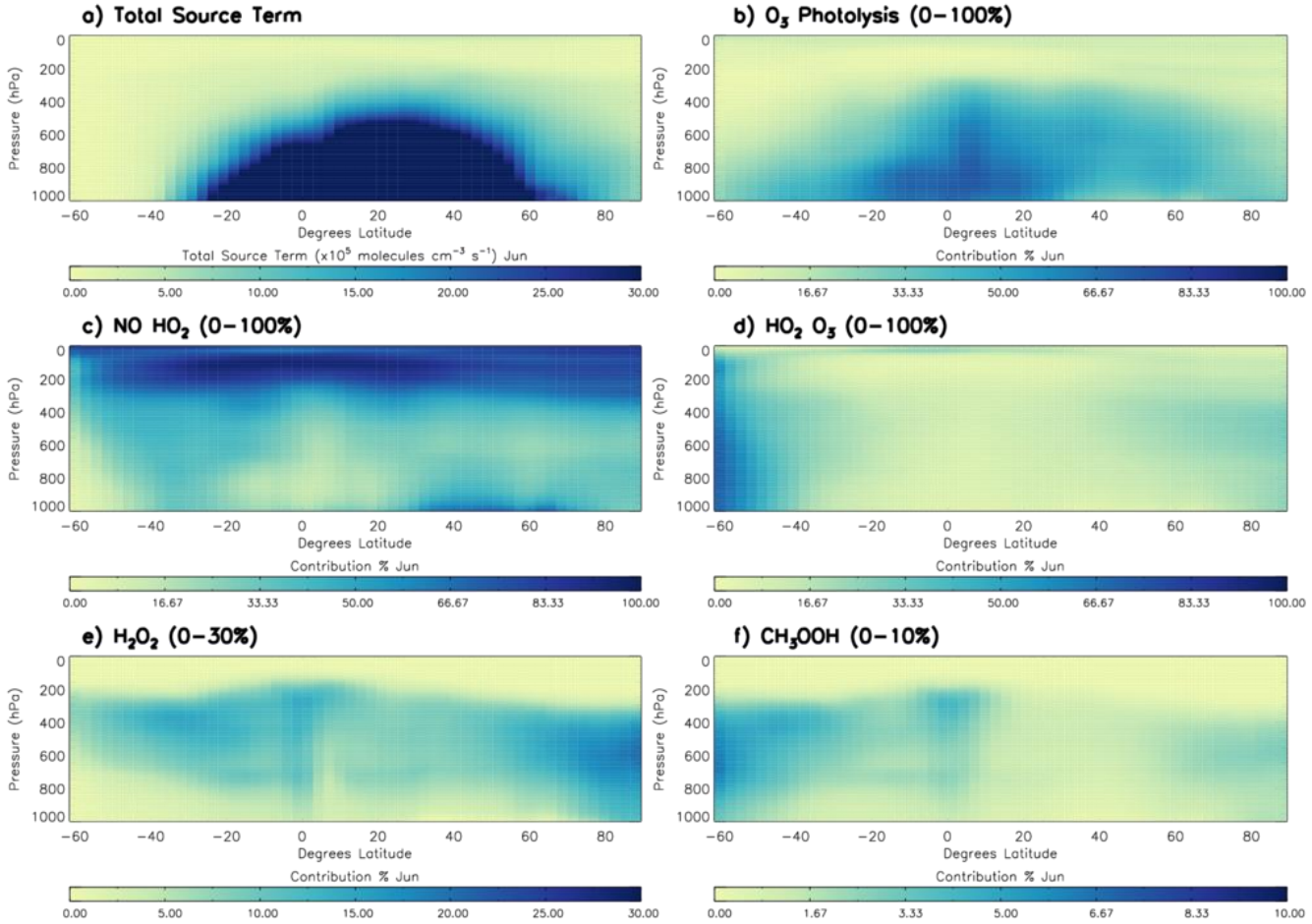


**Figure S12: June 2010 zonal mean global plots showing the total source term from the Sav-SSA and the different components as a % of total. The terms are: (a) total source, (b) photolysis of $O_3$ to form $O(^1D)$ which reacts with $H_2O$ for form OH, (c) reaction of NO and $HO_2$, (d) reaction of $HO_2$ and $O_3$, (e) photolysis of $H_2O_2$ and (f) photolysis of $CH_3OOH$. The data is presented from 60° S–90° N due to several species being zero below 60° S because of polar night at these latitudes during June.**

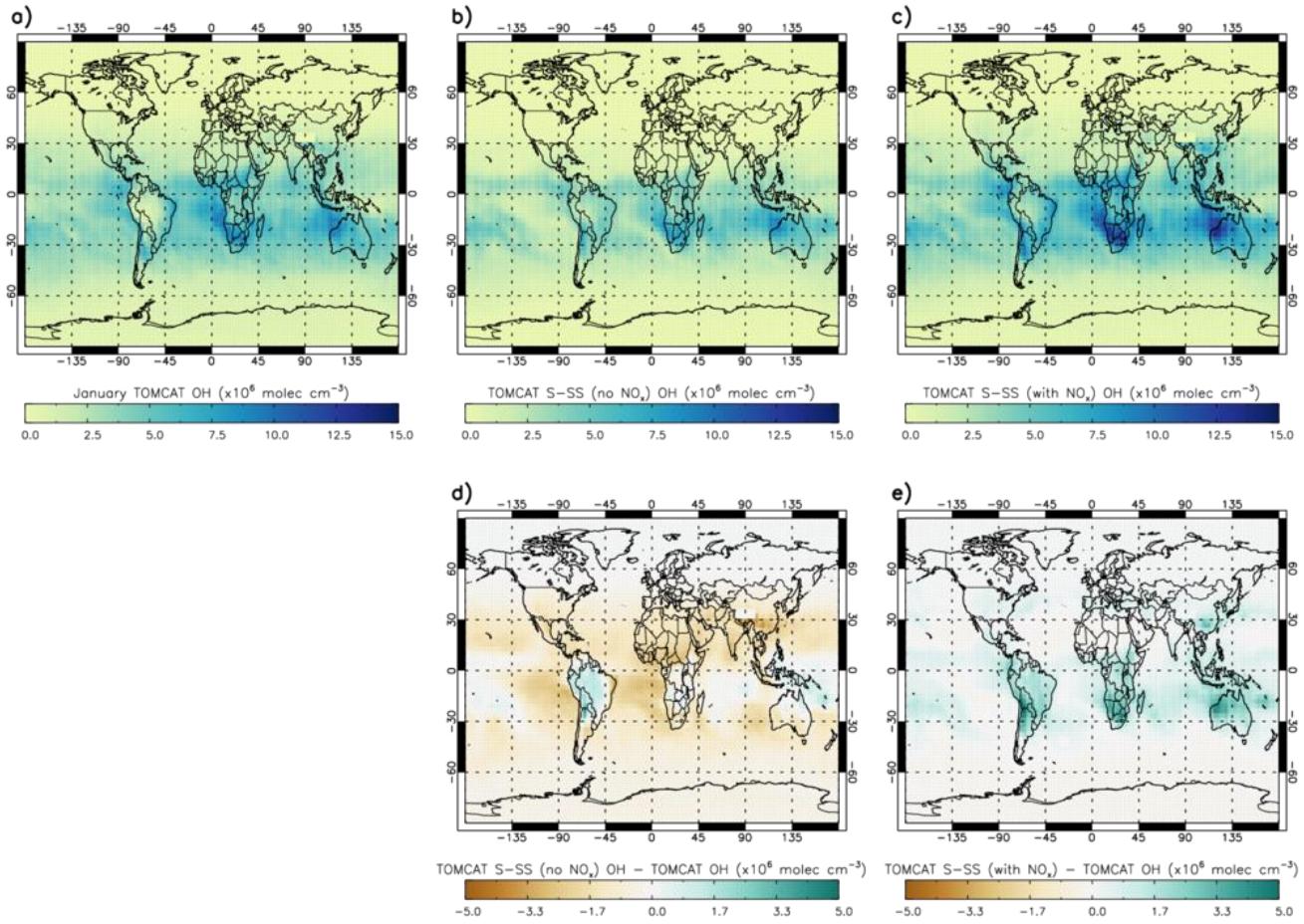


**Figure S13: Latitude-longitude plots of (a) TOMCAT [OH], (b) S-SSA [OH], (c) S-SSA with $NO_x$ sources/sinks (NO + $HO_2$, NO + OH + M, $NO_2$ + OH + M), (d) difference between S-SSA [OH] and TOMCAT [OH] and (e) difference between S-SSA [OH] with $NO_x$ sources/sinks and TOMCAT [OH]. All values are averaged for the 600-700 hPa pressure region for January in 2010 and in units of $\times 10^6$ molecule $cm^{-3}$.**

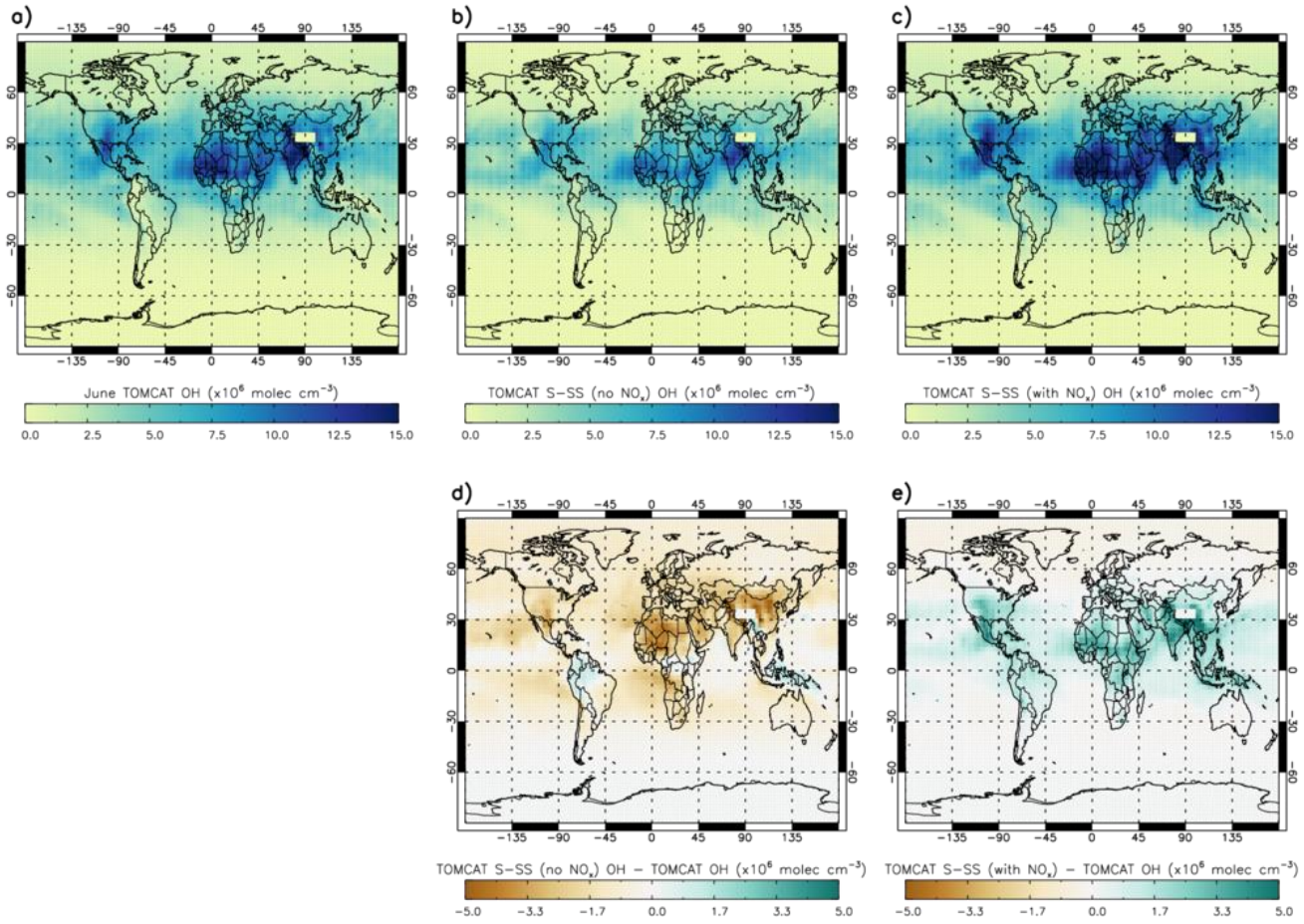


**Figure S14: Latitude-longitude plots of (a) TOMCAT [OH], (b) S-SSA [OH], (c) S-SSA with $NO_x$ sources/sinks (NO + $HO_2$, NO + OH + M, $NO_2$ + OH + M), (d) difference between S-SSA [OH] and TOMCAT [OH] and (e) difference between S-SSA [OH] with $NO_x$ sources/sinks and TOMCAT [OH]. All values are averaged for the 600-700 hPa pressure region for June in 2010 and in units of $\times 10^6$ molecule $cm^{-3}$.**

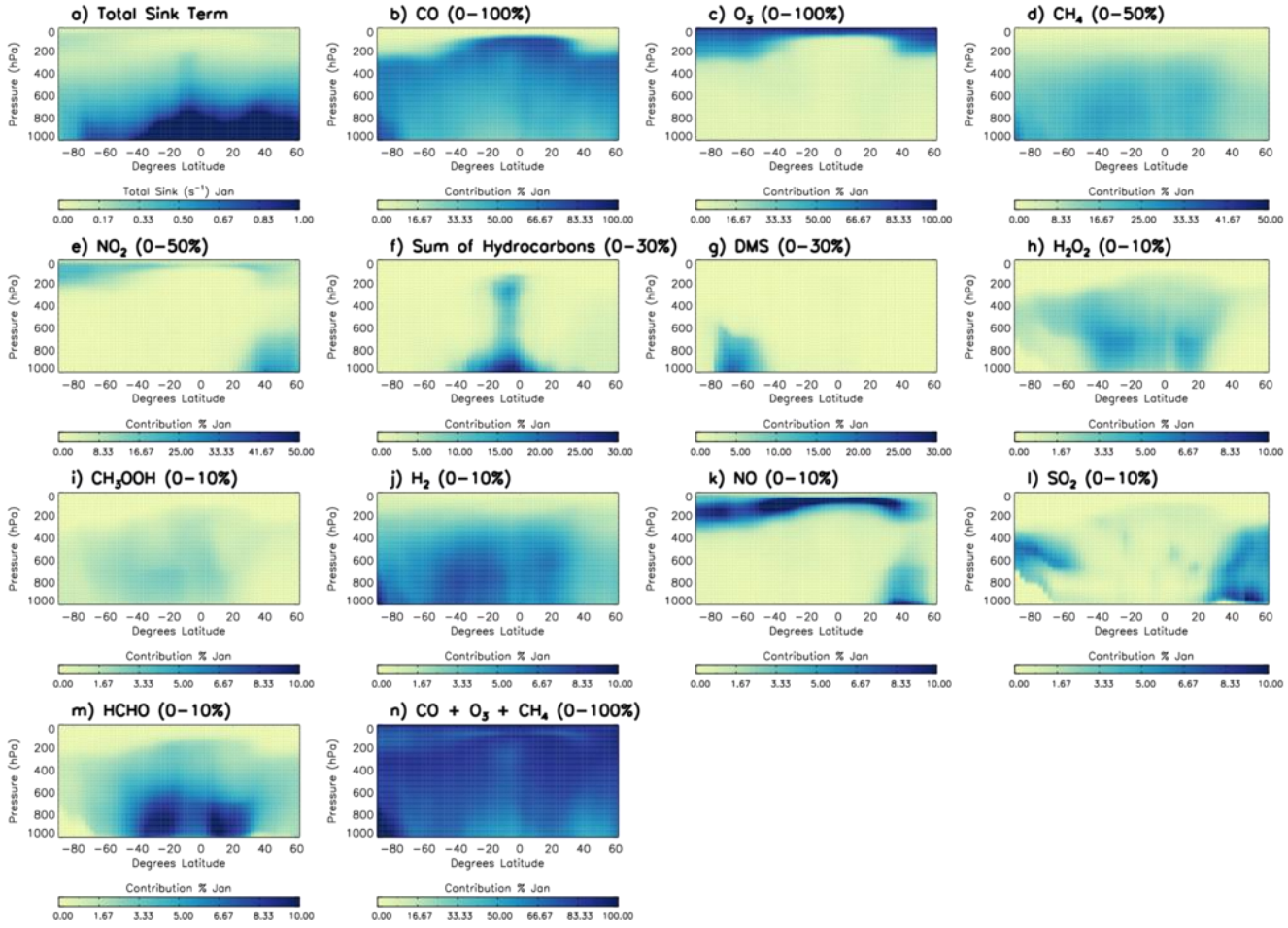


235

**Figure S15: January 2010 zonal mean global plots showing the total sink term from the Sav-SSA and the different components as a % of total. Panel (a) is the total sink. The other panels are the reaction of different species with OH: b) CO, (c) $O_3$, (d) $CH_4$, (e) $NO_2$, (f) sum of hydrocarbons ($C_2H_4$, $C_2H_6$, $C_3H_6$, $C_3H_8$, $C_5H_8$, $C_4H_{10}$), (g) dimethyl sulfide (DMS), (h) $H_2O_2$, (i) $CH_3OOH$, (j) $H_2$, (k) NO, (l) $SO_2$, (m) HCHO and (n) sum of CO, $O_3$ and $CH_4$ (denominator of main manuscript Eq. (4)). The data is presented from**
240 **90° S–60° N due to several species being zero poleward of 60° N as it is polar night at these latitudes during January.**

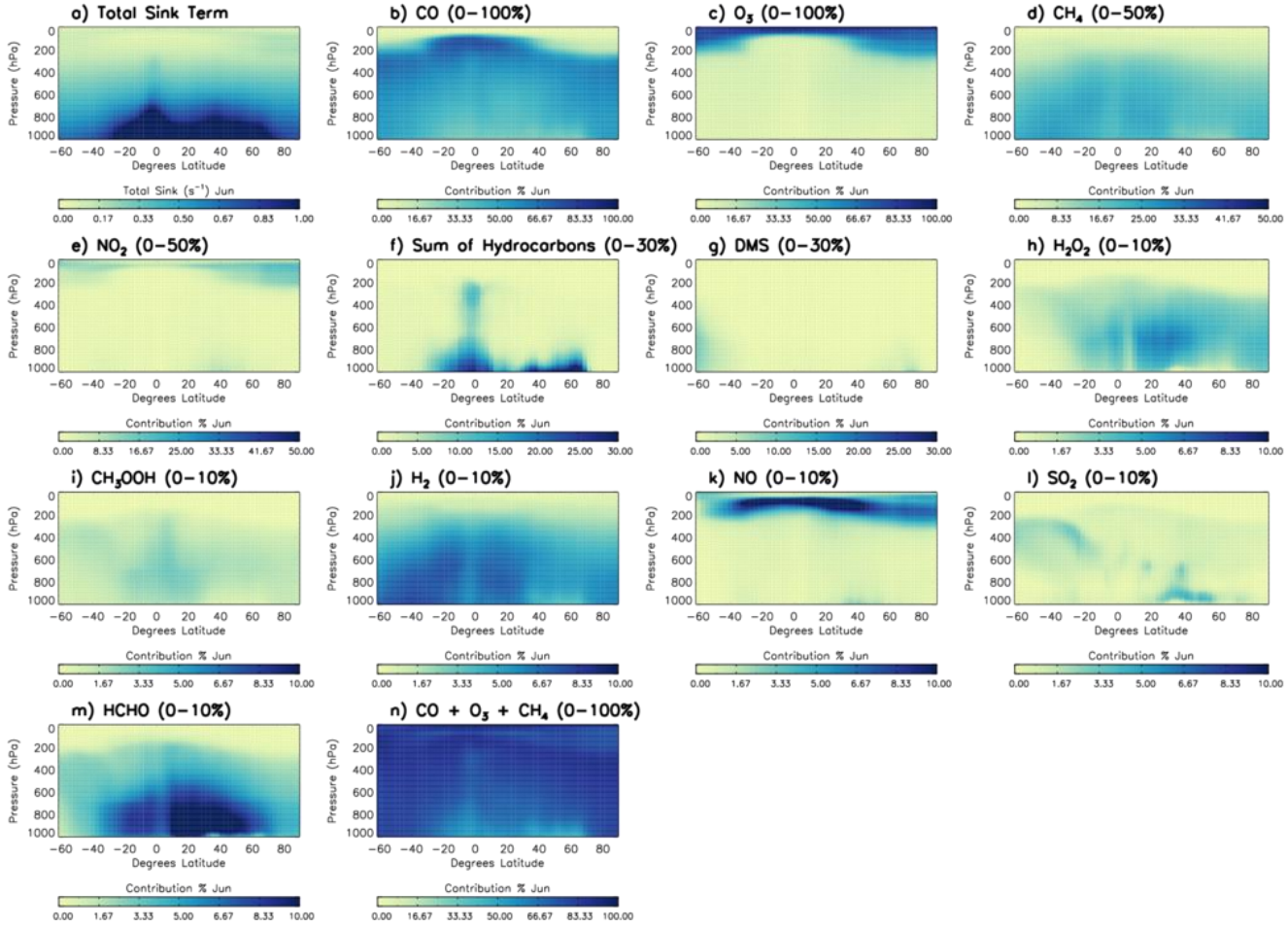


**Figure S16: June 2010 zonal mean global plots showing the total sink term from the Sav-SSA and the different components as a % of total. Panel (a) is the total sink. The other panels are the reaction of different species with OH: b) CO, (c) $O_3$, (d) $CH_4$, (e) $NO_2$, (f) sum of hydrocarbons ($C_2H_4$, $C_2H_6$, $C_3H_6$, $C_3H_8$, $C_5H_8$, $C_4H_{10}$), (g) dimethyl sulfide (DMS), (h) $H_2O_2$, (i) $CH_3OOH$, (j) $H_2$, (k) NO, (l) $SO_2$, (m) HCHO and (n) sum of CO, $O_3$ and $CH_4$ (denominator of main manuscript Eq. (4)). The data is presented from 60° S–90° N, several species being zero poleward of 60° S because of polar night at these latitudes during June.**

## Section S9. Impact of $NO_x$ source/sink terms of aircraft calculated OH

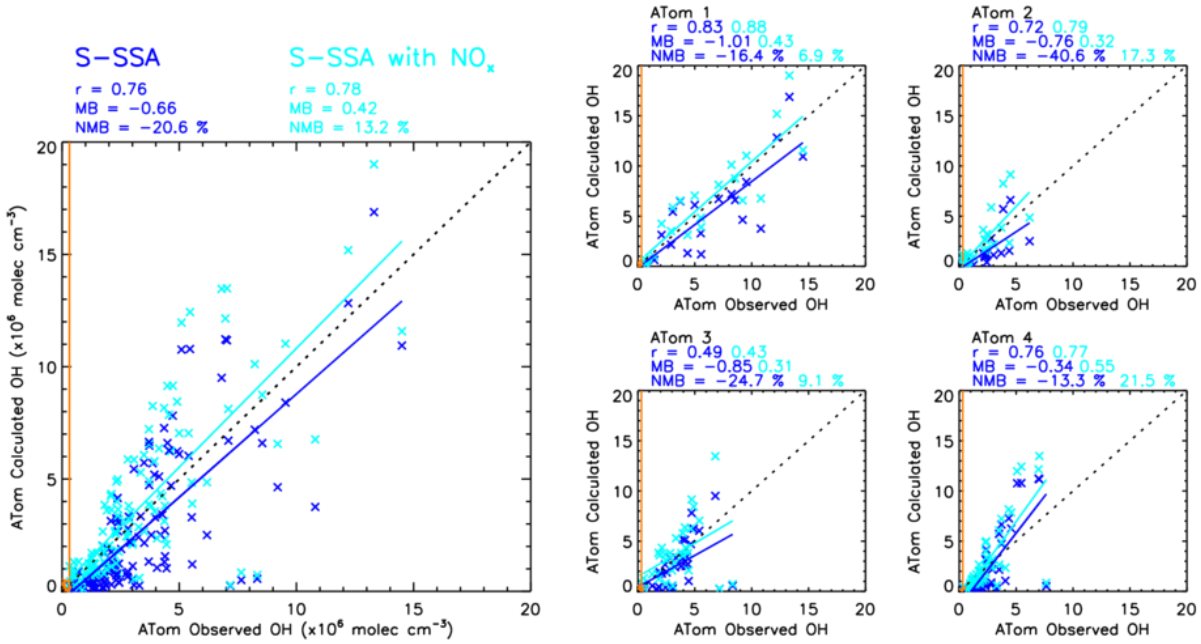


**Figure S17: Comparison between OH-calc and OH-obvs for the S-SSA with and without $NO_x$ reactions (NO + $HO_2$, NO + OH + M, $NO_2$ + OH + M). The left panel shows a combination of ATom-1, ATom-2, ATom-3 and ATom-4. The right four panels show the data split into the individual campaigns. ATom observations are filtered for 600–700 hPa and 08:00–11:00 LT. All data is in units of $\times 10^6$ molecule $cm^{-3}$. Data points in orange are excluded from the analysis, either as an outlier ( > mean + 3.0 standard deviations) or below the limit of detection of the ATHOS instrument (0.018 pptv or 0.31 $\times 10^6$ molecule $cm^{-3}$) shown by the orange line. Pearson's correlation co-efficient (r), the mean bias (calculated from OH-calc – OH-obvs) and the normalised mean bias (% with respect to OH-obvs) are displayed in the top left corner of each panel.**

**Section S10. OH reactivity**

OHR observations can potentially be used to check the denominator of a steady-state approximation, in this case a simplified expression for OHR (Eq. (5) in the main manuscript). Figure S18 shows a comparison of ATom OHR observations (OHR-obvs) and ATom data used in the simplified expression of OHR (OHR-calc) where ATom data was available for all species. The number of OHR observations available in the pressure interval of interest (600–700 hPa) is limited; ranging from only 11–17 in total per campaign in Fig. S18. Across all four ATom campaigns there is a bias of -36.7 % between OHR-obvs and OHR-calc. For the four individual campaigns (Fig. S18 RHS), it ranges between -57.6 % and +20.1 %. A negative bias is found for ATom-1, ATom-2 and ATom-3, whereas a positive bias is found for ATom-4. Across the four ATom campaigns the Pearson's correlation co-efficient is -0.02 for OHR-obvs and OHR-calc. For the individual four campaigns, this ranges between -0.23 and +0.20. Overall, there is a poor correlation, although OH-calc falls within the large 0.8 $s^{-1}$ uncertainty of OH-obvs for 80 % of the data points. Figure S19 shows a comparison between latitude-averaged OH-obvs (OHR-obvs-lat) and latitude-averaged OH-calc (OHR-calc-lat). Figure S19 shows that ~75 % of OHR-calc-lat values are within the large uncertainty of the OHR-obvs-lat (0.8 $s^{-1}$) across the four campaigns. Most of the ~25 % exceptions to this occur in the NH, the largest being -1.6 $s^{-1}$ in ATom-1, as well as one exceedance of the 0.8 $s^{-1}$ uncertainty in the SH with a bias of -2.9 $s^{-1}$.

The study by Travis et al. (2020) of ATom-1 and ATom-2 showed a substantial difference between OHR calculated from observed reactants and OHR observations below 3–4 km altitude. This difference is present in both the NH and SH, in an altitude range from ~4 km to surface for ATom-1, and ~3 km to the surface for ATom-2. The pressure range of 700–600 hPa equates to roughly 3–4 km altitude, so our finding that the OHR-obvs in ATom-2 (NMB = -24 %) agree better with OHR-calc than in ATom-1 (NMB = -51 %) is consistent with Travis et al. (2020) The higher OHR observations in comparison to OHR calculated from observed reactants near the surface is a well-studied area, usually called "OH missing reactivity". In our study the missing reactivity has an average of 0.34 $s^{-1}$ and peaks at 2.9 $s^{-1}$ across the four ATom campaigns. This is similar to the findings of Thames et al. (2020) who found that for ATom-1, 2 and 3 the missing reactivity in the marine boundary layer varied between 0 and 3.5 $s^{-1}$, with an average of 0.5 $s^{-1}$.

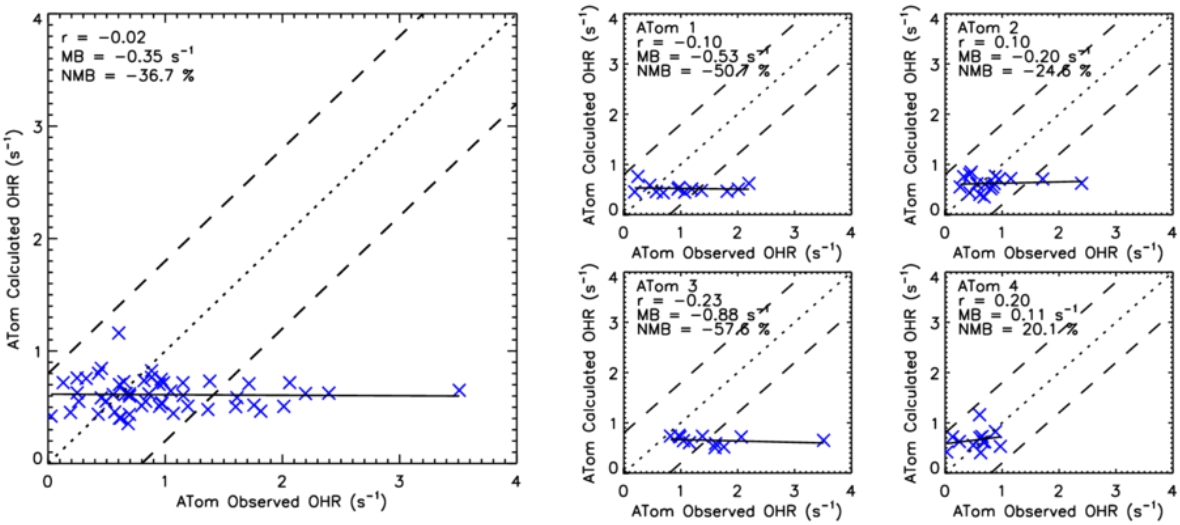


285

**Figure S18: Comparison between OHR-calc and OHR-obvs. The left panel shows a combination of ATom-1, ATom-2, ATom-3 and ATom-4. The 4 right panels show the data split into the individual campaigns. The dashed lines represent the ± OHR uncertainty (corresponding to the ± 0.8 $s^{-1}$ uncertainty in the measurements) and the dotted lines show the 1:1 line. ATom observations are filtered for 600–700 hPa and 08:00–11:00 local time.**

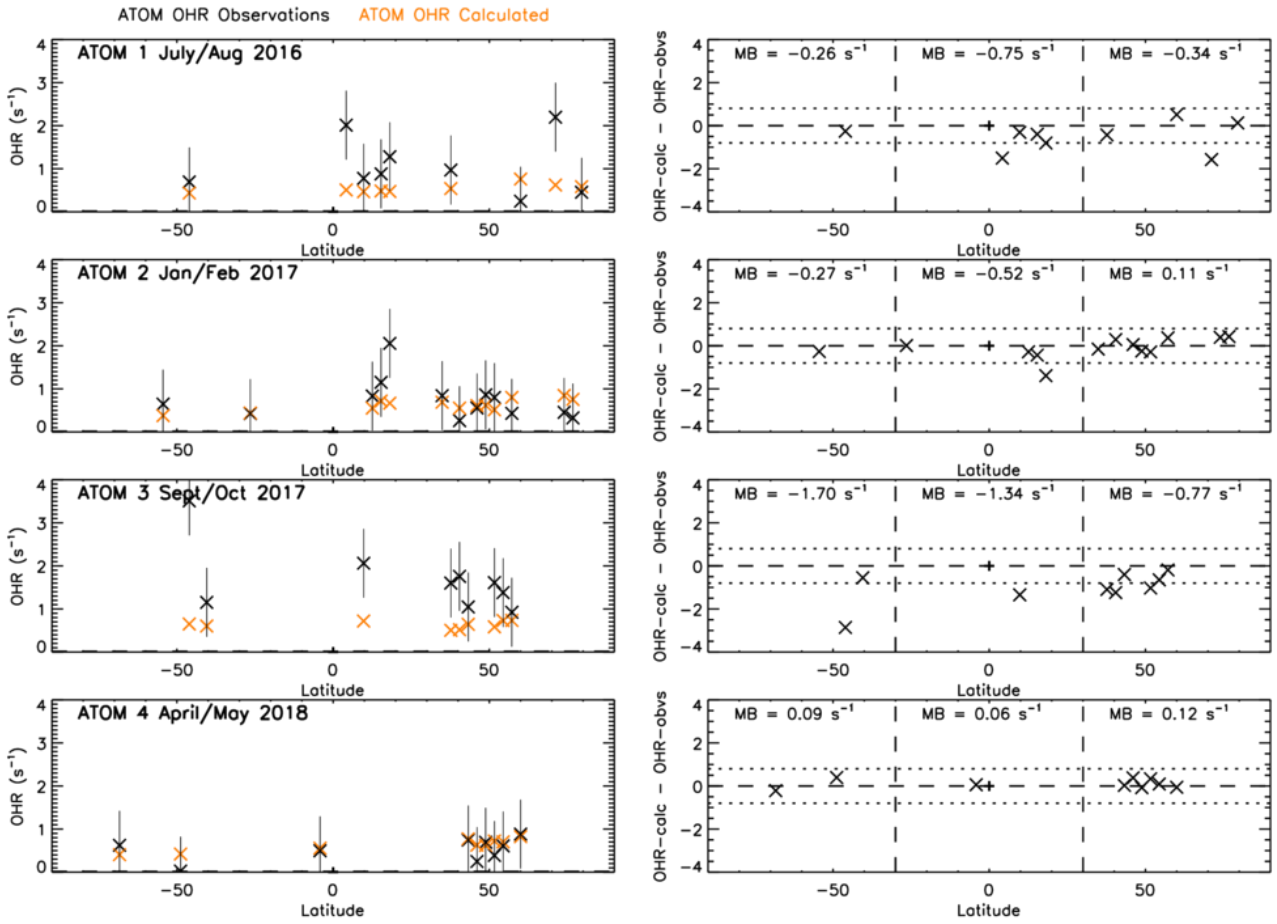


**Figure S19: OHR-calc and OHR-obvs comparison for the 4 ATom campaigns. Left panels show latitude averaged OHR ($s^{-1}$) with error bars of ± 0.8 $s^{-1}$. Right panels show latitude-averaged OHR difference between OHR-obvs and OHR-calc ($s^{-1}$) with the mean difference (MB) labelled for 3 different latitude regions (90°–30° S, 30° S–30° N and 30°–90° N). The dotted line represents the ± 0.8 $s^{-1}$ uncertainty in the observations. ATom observations are filtered for 600–700 hPa and 08:00–11:00 local time.**

**Section S11. Temperature and input species anomalies relative to a 2008–2017 average**

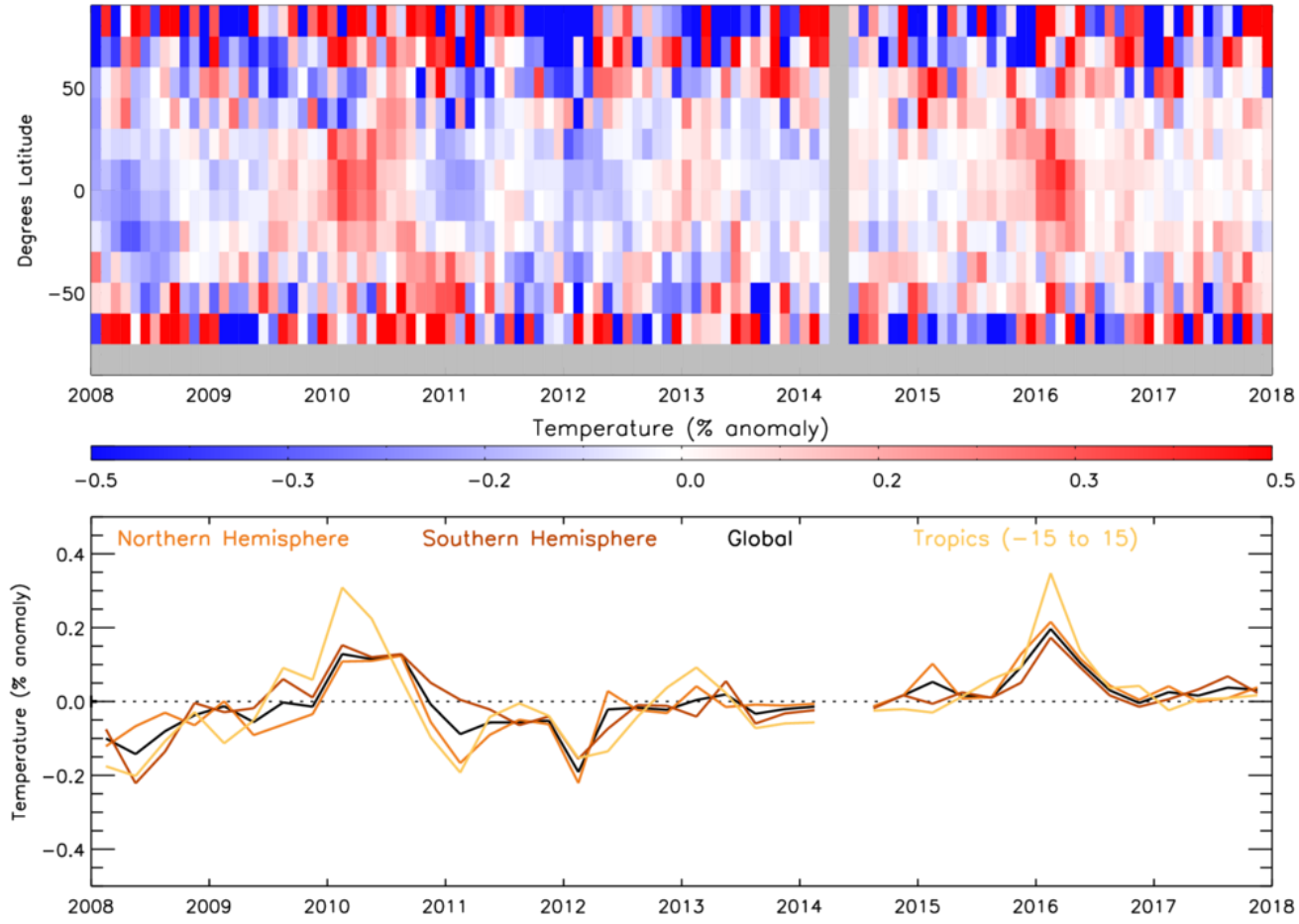


**Figure S20: Monthly mean satellite temperature anomaly (%) (2008–2017): (a) 15° latitude bins and (b) 3-month average global, NH, SH and tropics means. Anomaly is relative to a 2008–2017 average.**

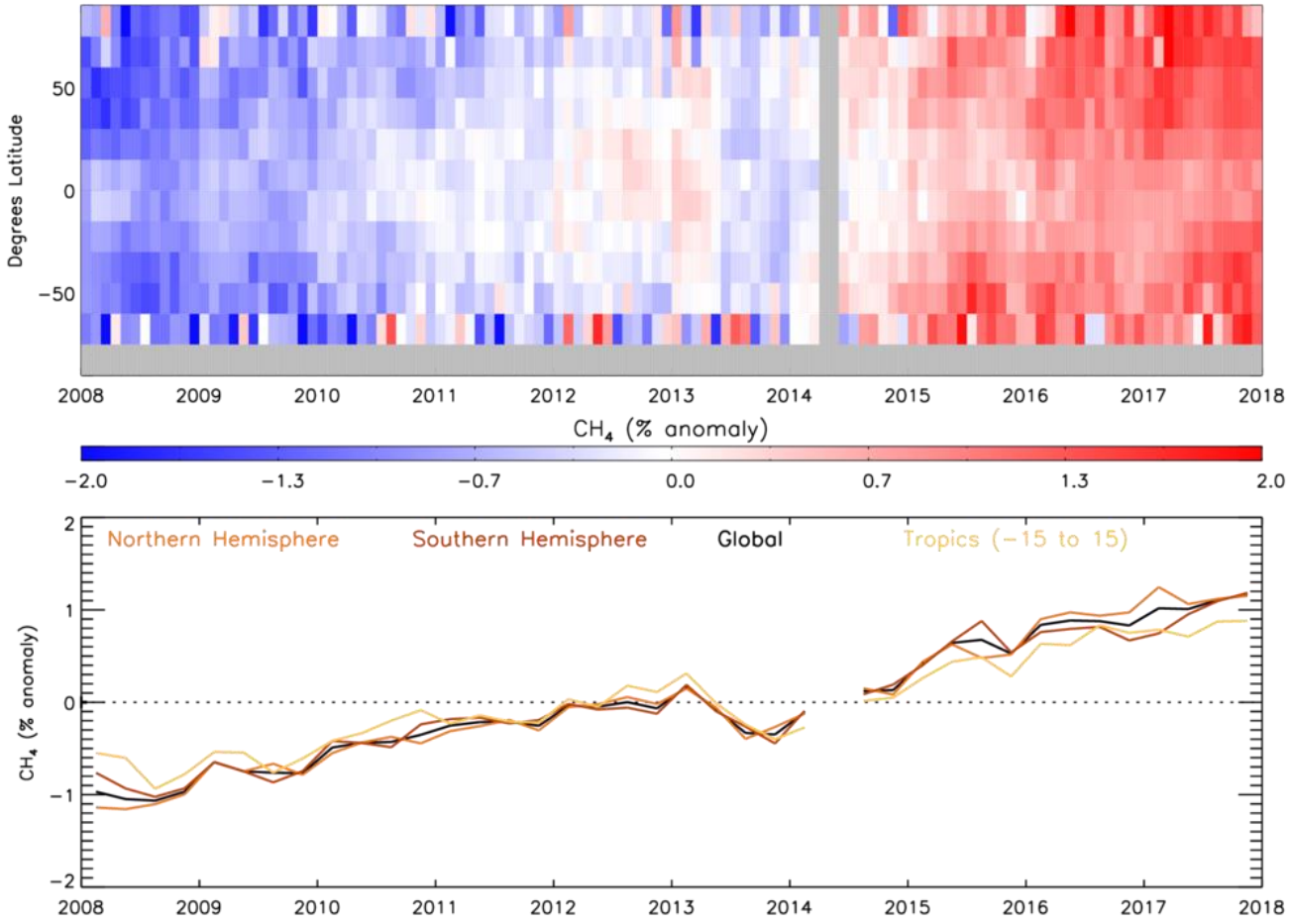


**Figure S21: Monthly mean satellite $CH_4$ anomaly (%) (2008–2017): (a) 15° latitude bins and (b) 3-month average global, NH, SH and tropics means. Anomaly is relative to a 2008–2017 average.**

305

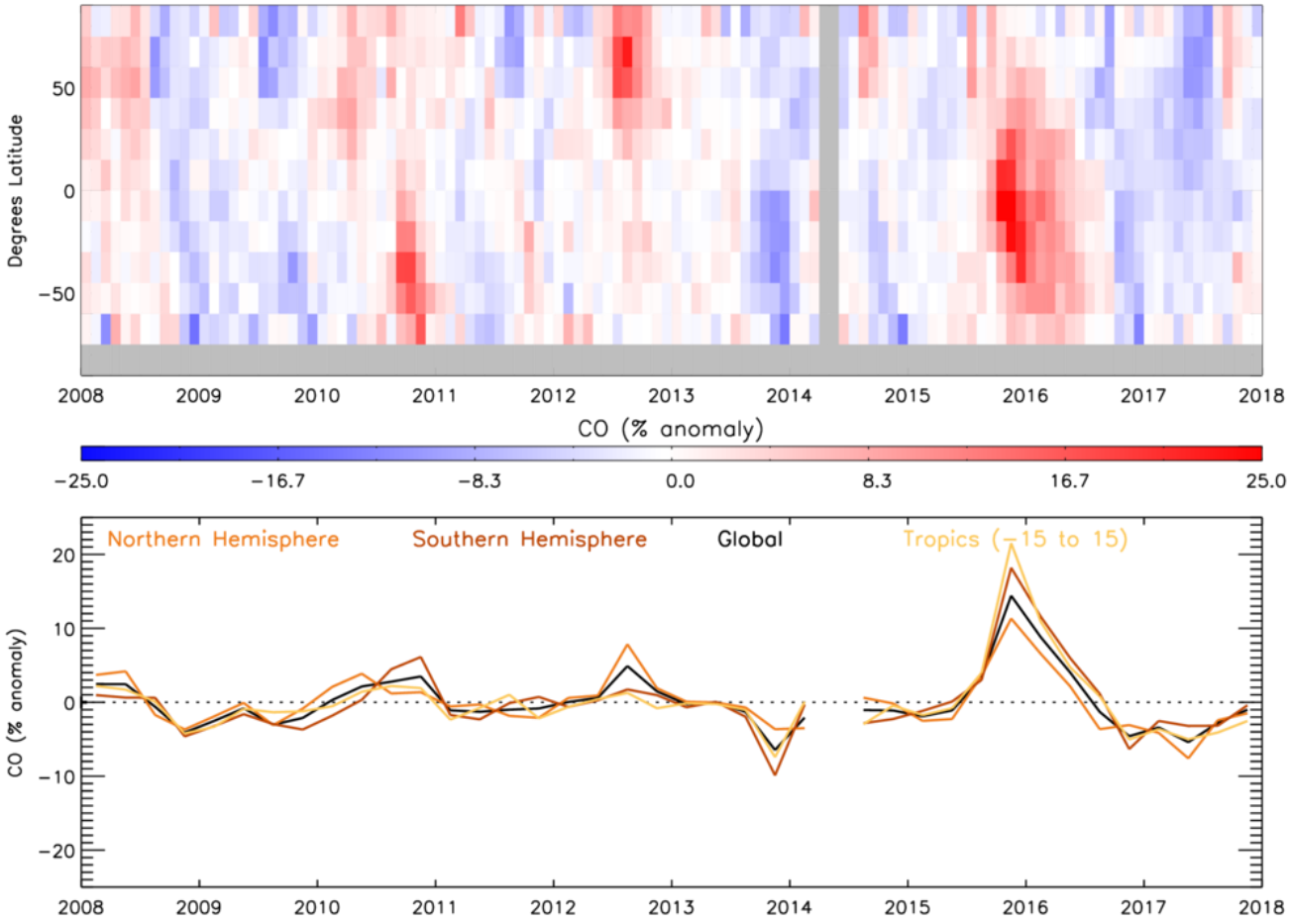


**Figure S22: Monthly mean satellite CO anomaly (%) (2008–2017): (a) 15° latitude bins and (b) 3-month average global, NH, SH and tropics means. Anomaly is relative to a 2008–2017 average.**

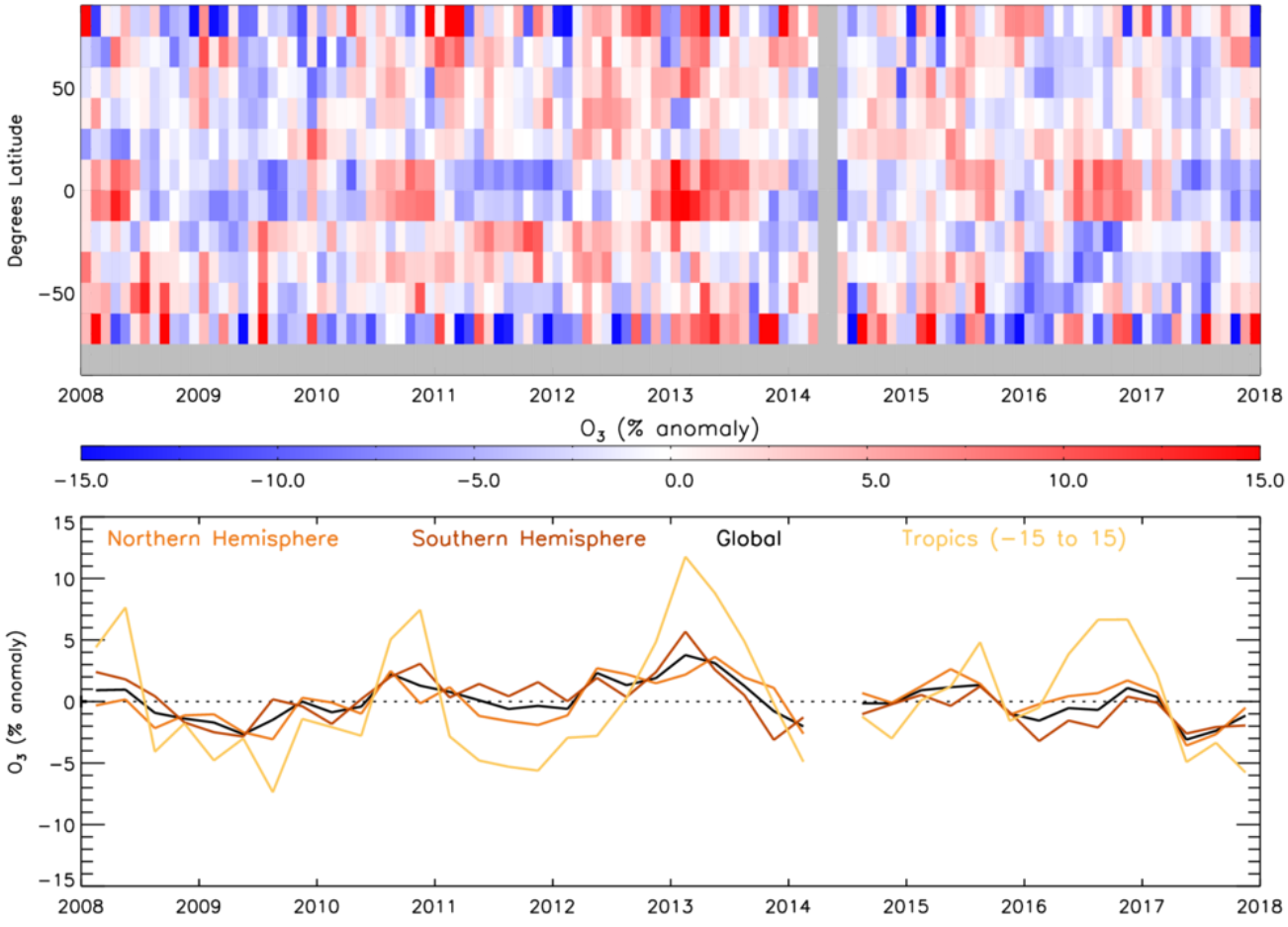


**Figure S23: Monthly mean satellite $O_3$ anomaly (%) (2008–2017): (a) 15° latitude bins and (b) 3-month average global, NH, SH and tropics means. Anomaly is relative to a 2008–2017 average.**

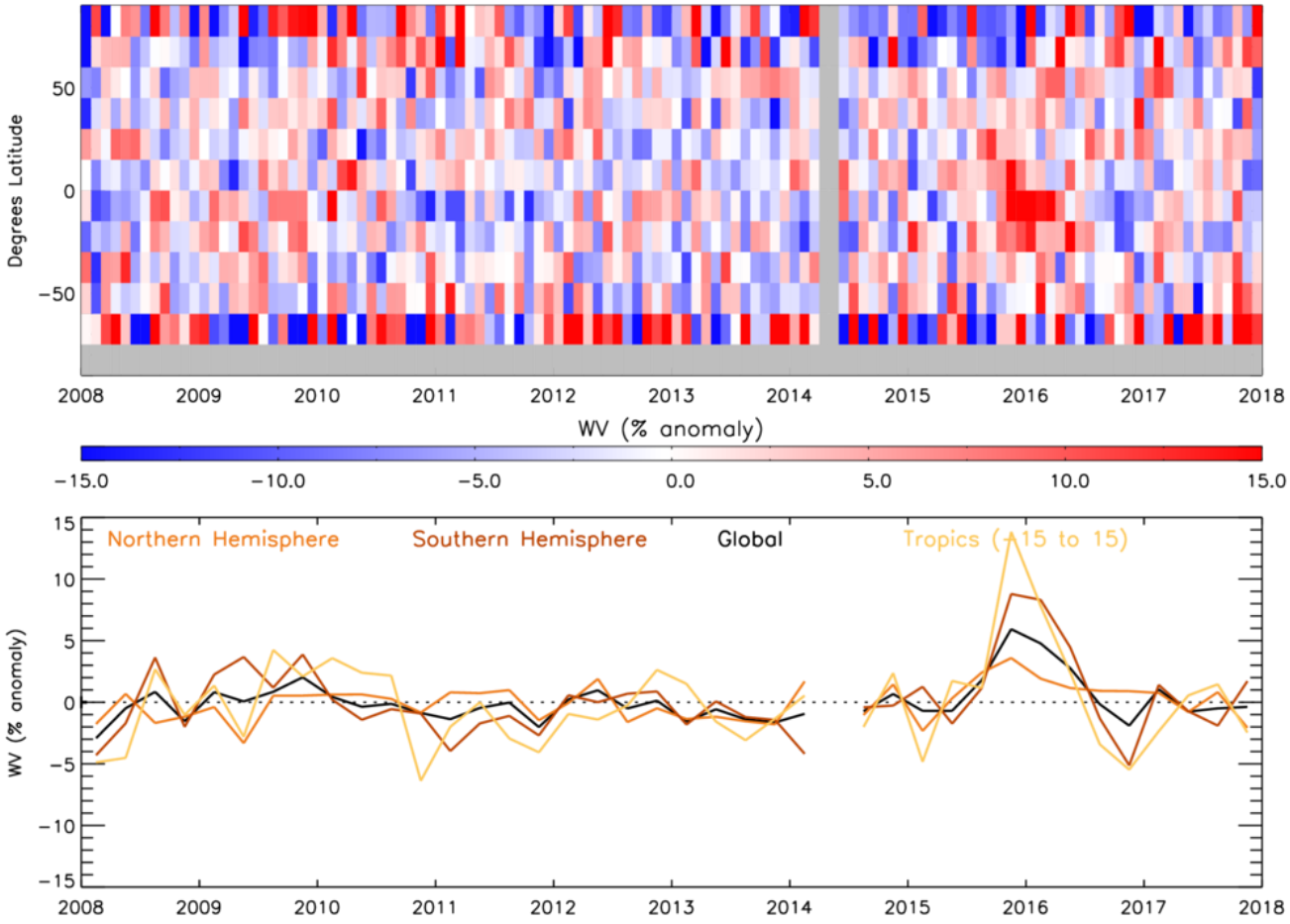


315 **Figure S24: Monthly mean satellite water vapour anomaly (%) (2008–2017): (a) 15° latitude bins and (b) 3-month average global, NH, SH and tropics means. Anomaly is relative to a 2008–2017 average.**

**References**


Hogan, R.: How to combine errors, [online] Available from: http://cree.reading.ac.uk/~swrhgnrj/combining_errors.pdf (Accessed 1 December 2021), 2006.

Monks, S. A., Arnold, S. R., Hollaway, M. J., Pope, R. J., Wilson, C., Feng, W., Emmerson, K. M., Kerridge, B. J., Latter, B. L., Miles, G. M., Siddans, R. and Chipperfield, M. P.: The TOMCAT global chemical transport model v1.6: Description of chemical mechanism and model evaluation, Geosci. Model Dev., doi:10.5194/gmd-10-3025-2017, 2017.

Pope, R. J., Kerridge, B. J., Siddans, R., Latter, B. G., Chipperfield, M. P., Arnold, S. R., Ventress, L. J., Pimlott, M. A., Graham, A. M., Knappett, D. S. and Rigby, R.: Large enhancements in southern hemisphere satellite-observed trace gases due to the 2019/2020 Australian wildfires, J. Geophys. Res. Atmos., 1–13, doi:10.1029/2021jd034892, 2021.

Pöschl, U., Von Kuhlmann, R., Poisson, N. and Crutzen, P. J.: Development and Intercomparison of Condensed Isoprene Oxidation Mechanisms for Global Atmospheric Modeling, J. Atmos. Chem., 31(1), 29–52, doi:10.1023/A:1006391009798, 2000.

Savage, N. H., Harrison, R. M., Monks, P. S. and Salisbury, G.: Steady-state modelling of hydroxyl radical concentrations at Mace Head during the EASE ’97 campaign, May 1997, Atmos. Environ., doi:10.1016/S1352-2310(00)00315-0, 2001.

Shetter, R. E. and Müller, M.: Photolysis frequency measurements using actinic flux spectroradiometry during the PEM-Tropics mission: Instrumentation description and some results, J. Geophys. Res. Atmos., 104(D5), 5647–5661, doi:10.1029/98JD01381, 1999.

Siddans, R., Knappett, D., Kerridge, B., Waterfall, A., Hurley, J., Latter, B., Boesch, H. and Parker, R.: Global height-resolved methane retrievals from the Infrared Atmospheric Sounding Interferometer (IASI) on MetOp, Atmos. Meas. Tech., 10(11), 4135–4164, doi:10.5194/amt-10-4135-2017, 2017.

Thames, A. B., Brune, W. H., Miller, D. O., Allen, H. M., Apel, E. C., Blake, D. R., Paul Bui, T., Commane, R., Crounse, J. D., Daube, B. C., Diskin, G. S., Digangi, J. P., Elkins, J. W., Hall, S. R., Hanisco, T. F., Hannun, R. A., Hintsa, E., Hornbrook, R. S., Kim, M. J., McKain, K., Moore, F. L., Nicely, J. M., Peischl, J., Ryerson, T. B., St. Clair, J. M., Sweeney, C., Teng, A., Thompson, C. R., Ullmann, K., Wennberg, P. O. and Wolfe, G. M.: Missing OH reactivity in the global marine boundary layer, Atmos. Chem. Phys., 20(6), 4013–4029, doi:10.5194/acp-20-4013-2020, 2020.

Travis, K., Heald, C., Allen, H., Apel, E., Arnold, S., Blake, D., Brune, W., Chen, X., Commane, R., Crounse, J., Daube, B., Diskin, G., Elkins, J., Evans, M., Hall, S., Hintsa, E., Hornbrook, R., Kasibhatla, P., Kim, M., Luo, G., McKain, K., Millet, D., Moore, F., Peischl, J., Ryerson, T., Sherwen, T., Thames, A., Ullmann, K., Wang, X., Wennberg, P., Wolfe, G. and Yu, F.: Constraining remote oxidation capacity with ATom observations, Atmos. Chem. Phys. Discuss., (January), 1–41, doi:10.5194/acp-2019-931, 2020.